Table of Contents

I. FISCHER-TROPSCH SYNTHESIS ON IRON CATALYSTS

1. Background

1.1. Structure and Function of Active Phases in Fischer-Tropsch Synthesis

Fe-based oxides have been used as commercial catalysts for Fischer-Tropsch synthesis (FTS) to produce a large variety of paraffin and olefin products, ranging from methane to high molecular weight waxes [1]. During activation by synthesis gas and subsequent FTS reaction, several phases including metallic iron, iron carbides and iron oxides are known to co-exist at steady-state conditions [2-5]. The distribution and amounts of these phases depend on exposure to various activation and reaction conditions, leading to different catalytic performances in FTS. Some researchers [6] have proposed that surface iron atoms are responsible for FTS activity, while some others considered surface carbides or a mixture of carbides [7,8] and metallic iron [9] to be the active phase. There are also some reports that suggest that magnetite Fe_3O_4 is the active phase in FTS [10-12]. Although these studies have each provided some evidence to support their specific proposals about the active phase, the available information remains phenomenological, and a method to identify the active phase during reaction and to count the number of active sites has not yet been established.

Based on the previous research on Co [13,14] and Fe catalysts [15,16] for FTS as well as our last quarterly work on TPSR of Fe oxides in H_2, our characterization during this research period involved temperature-programmed reactions of Fe-based catalysts with flowing streams of CO or H_2-CO mixtures. We monitored the gas phase concentrations throughout the reduction and carburization processes by means of an on-line mass spectrometer, and followed the evolution of bulk phases and crystal size by X-ray diffraction and of surface area by nitrogen physisorption measurements. In this way, we can determine the temperature required for the formation of Fe carbides as well as the stoichiometry and structure of such carbides. Our goal is to develop a new synthesis method to improve the compositional and structural purity of Fe carbides formed, and consequently to refine the structure-function relationships that we have previously proposed to interpret the catalytic behavior of Fe-based catalysts.

1.2. Effects of Zn, K and Cu

Many components have been added to Fe catalysts in order to improve their mechanical and catalytic properties. Our previous studies have shown that zinc, alkali and copper [16,17] promote the catalytic properties of Fe oxides. Zinc oxide, as a non-reducible oxide in FTS conditions, appears to stabilize the surface area of Fe oxide. Alkali, as a modifier of the adsorption enthalpies of H_2 and CO, increases the selectivity to desired C_{5+} products. Copper promotes the carburization processes and decreases the temperature required for the activation of iron oxide. Here, our efforts have focused on Fe-Zn-K-Cu catalysts. We have prepared a series of Zn and Fe co-precipitated oxides with varied Zn/Fe ratios and then introduced varying amounts of K and Cu. We are examining the surface area, bulk structure, required reduction and carburization temperatures as well as the catalytic behavior of these catalysts, in order to identify optimum Zn/Fe ratios and Cu and K contents that give maximum site density and catalytic activity.

2. Synthesis Procedures for Fe-Zn-K-Cu Oxides

All catalysts were prepared by co-precipitation of zinc and iron nitrates at a constant pH of 7.0 in order to to form porous mixed oxides. Then, these oxide precursors were impregnated with an aqueous solution of potassium and copper salts using incipient wetness methods. The Zn/Fe oxide precursors were prepared first. Fe nitrate (1.4 M) and Zn nitrate (3.0 M) solutions were mixed at a given atomic Zn/Fe ratio. A solution of ammonium carbonate (1 M) was prepared separately. Deionized water (ca. 50 ml) was added into a large flask, which was heated on a hot plate with a magnetic stirrer and held at 80 ^{o}C throughout the preparation process. The mixed Zn/Fe solution was added at 2 cm^{3}/min flow into the flask through a feeding pump. At the same time, the ammonium carbonate solution was fed separately, and its flow was controlled to maintain the slurry pH at 7±0.1, as monitored by a pH meter. The resulting precipitates were washed several times with about 1 l water per gram of catalyst, dried at 120 ^{o}C overnight, and then calcined at 350 ^{o}C for 1 h. The calcined material was promoted with 2 at.% K using K$_2$CO$_3$ solution (0.16 M) by incipient wetness and then dried. The same process was repeated in order to promote samples with 1 at.% Cu using Cu(NO$_3$)$_2$ solutions (0.16 M). Finally, the dried material was treated in dry air at 400 ^{o}C for 4 h. This final calcination temperature was chosen from temperature-programmed oxidation data, which showed that this temperature is sufficient to decompose all metal nitrates and carbonates except K$_2$CO$_3$. The catalysts contain CuO, ZnO, Fe$_2$O$_3$ and K$_2$CO$_3$. These catalysts were pressed at 443 MPa into pellets, lightly crushed, and then sieved to retain the 80 - 140 mesh fraction for FTS reaction.

3. Catalyst Characterization

3.1. Protocols for the Characterization of Fe-based FTS Catalysts

This research program addresses the synthesis and the structural and catalytic characterization of the active sites of Fe-based catalysts for FTS. We have designed a matrix of samples that contains a systematic range of multi-components catalysts in order to determine the number and type of surface sites present on fresh catalysts and the samples after FTS reaction (Table 1.1). Our objective is to develop rigorous relationships between the synthesis methods, the resulting catalyst structures, and their function in FTS reactions.

3.2. In-Situ X-ray Absorption (XAS) Studies on Fe Catalysts

In-situ X-ray absorption near edge (XANES) and extended X-ray absorption fine structure (EXAFS) analyses provide us with the information about the oxidation states and the local structure of catalysts during FTS. In this reporting period, X-ray absorption measurements were carried out at the Stanford Synchrotron Radiation Laboratory (SSRL). We measured potassium K-edge spectra of Fe-Zn-K-Cu oxides and their carbides on beamline VI-2. Also, we measured *in-situ* Fe K-edge spectra of a typical Fe-Zn-K-Cu oxide (Zn/Fe=0.1, K/M=0.02, Cu/M=0.01, M=(Fe+Zn)) during TPR in H$_2$ on

Table 1.1. Matrix of Fe-Zn-K-Cu samples and characterization methods for FTS reaction

Composition of the Catalysts			Characterization Before and After FTS	FTS reaction
Zn/Fe mole ratio	K/(Fe+Zn) (at.%)	Cu/(Fe+Zn) (at.%)		
0	0	0	XRD Surface area In-situ XAS H_2-TPR CO-TPR (H_2+CO)-TPR	Effect of reaction condition 220 ^{o}C 21.4 atm 235 ^{o}C 21.4 atm 270 ^{o}C 5 atm Effect of CO_2 addition
0	0	1		
0	2	0		
0	2	1		
0	2	2		
0	4	1		
0.05	0	0		
0.05	2	1		
0.05	4	2		
0.1	0	0		
0.1	0	1		
0.1	2	0		
0.1	2	1		
0.1	2	2		
0.1	4	1		
0.2	0	0		
0.2	2	1		
0.2	4	2		
0.4	0	0		
0.4	0	1		
0.4	2	0		
0.4	2	1		
0.4	2	2		
0.4	6	1		

beamline VI-2, and the reduction and carbonization in CO and in synthesis gas on beamline II-3, respectively. Experiments were performed using a Si(111) monochromator crystal. X-ray absorption spectra were obtained in transmission mode. For potassium K-edge spectra, the solid samples were finely ground and sealed in a Prolene[TM] envelope and fixed in the plate window. Thickness effects were not a problem for K spectra measurements since the specimens contained about 2-4 at.% K. For *in-situ* Fe K-edge spectra, we diluted the samples with graphite powder to obtain 7 wt.% Fe. The samples were ground with graphite, pressed into pellets, and sieved to retain the 45-60 mesh fraction, and loaded into a quartz capillary cell for measurement as described in the previous quarterly report.

3.3   In-situ Fe K-edge XAS Measurement for Fe-Zn-K-Cu Oxide in H_2

3.3.1.   Fe K-Edge XANES

The Fe K-edge XANES spectra of Fe_2O_3, Fe_3O_4 and Fe foil are shown in Figure 1.1. The spectrum for Fe_2O_3 shows a strong absorption edge derived from the transition immediately above the threshold to the continuum, which is referred to as the white line. Fe_3O_4 shows a pre-edge peak below the absorption edge that is assigned to the *1s* to *3d* transition, and a sharp peak above the pre-edge derived from the transition of *1s* electron to continuum similar to that of Fe_2O_3. XANES spectrum for Fe metal shows a shoulder near the edge, but no white line. The XANES spectra of the Fe-Zn-K-Cu oxide (Zn/Fe=0.1, K/M=0.02, Cu/M=0.01, M=(Fe+Zn)) shows a pre-edge peak at 7.113 keV, reflecting a *1s* to *3d* electronic transition that is dipole-forbidden in centrosymmetric structures, but becomes allowed in tetrahedral or distorted octahedral structures because of p-d orbital mixing. Since the bulk phase of this Fe-Zn-K-Cu oxide is Fe_2O_3, and Zn is present in an amorphous form of $ZnFe_2O_4$, this pre-edge feature is most likely contributed by the presence of $ZnFe_2O_4$, where Fe occupies the distorted octahedral holes [20]. With an increase of temperature, the pre-edge features change and the absorption edges shift to lower energies. Above 280 ^{o}C, the spectra increasingly show more characteristic features of metallic Fe, suggesting that the oxide reduces.

3.3.2.   Fe K-Edge XANES Differential Spectra

Figure 1.2 shows the Fe K-edge XANES differential spectra of standard compounds Fe_2O_3, Fe_3O_4, and Fe, and in-situ spectra of the Fe-Zn-K-Cu oxide in H_2 with increasing temperatures. Fe_2O_3, Fe_3O_4 and Fe metal show Fe K-edge energies at 7.127, 7.125 and 7.112 keV, respectively. For the Fe-Zn-K-Cu oxide, beyond the pre-edge (7.113 keV), the spectrum presents the first inflection point at 7.123 keV, which is lower than that of Fe_2O_3 or Fe_3O_4. This suggests the presence of a low oxidation state species like FeO in this Fe-Zn-K-Cu oxide besides the predominant Fe_2O_3 bulk phase. With increasing reduction temperature, the Fe K-edge shifts to lower energies and significant reduction to metallic Fe occurs at temperatures above 280 ^{o}C. This reduction temperature appears to be about 70 ^{o}C lower than that obtained from our TPSR experiment for the H_2 temperature-programmed reduction, where the reduction to metallic Fe occurs at about 350 ^{o}C. Although we can not quite explain the temperature difference between the XAS

results and that of TSPR, the reduction trend is consistent with the results from TPSR experiments.
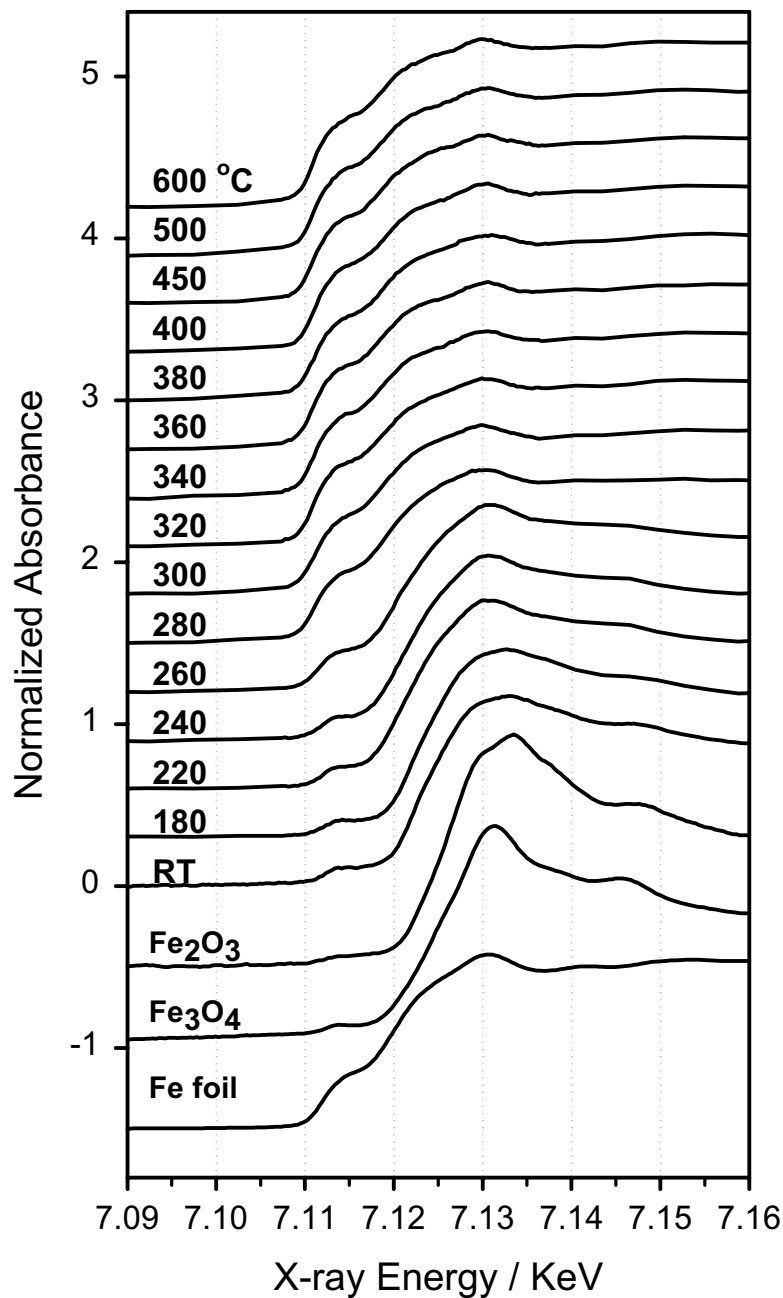

Figure 1.1. Fe K-edge XANES spectra of Fe standard compounds: Fe_2O_3, Fe_3O_4 and Fe foil; *In-situ* Fe K-edge XANES spectra of a Fe-Zn-K-Cu oxide (Zn/Fe=0.1, K/M=0.02, Cu/M=0.01, M=(Fe+Zn)) in H_2 (8 mg sample; 7 wt.% Fe; 5 cm^3/min H_2) at different temperatures.
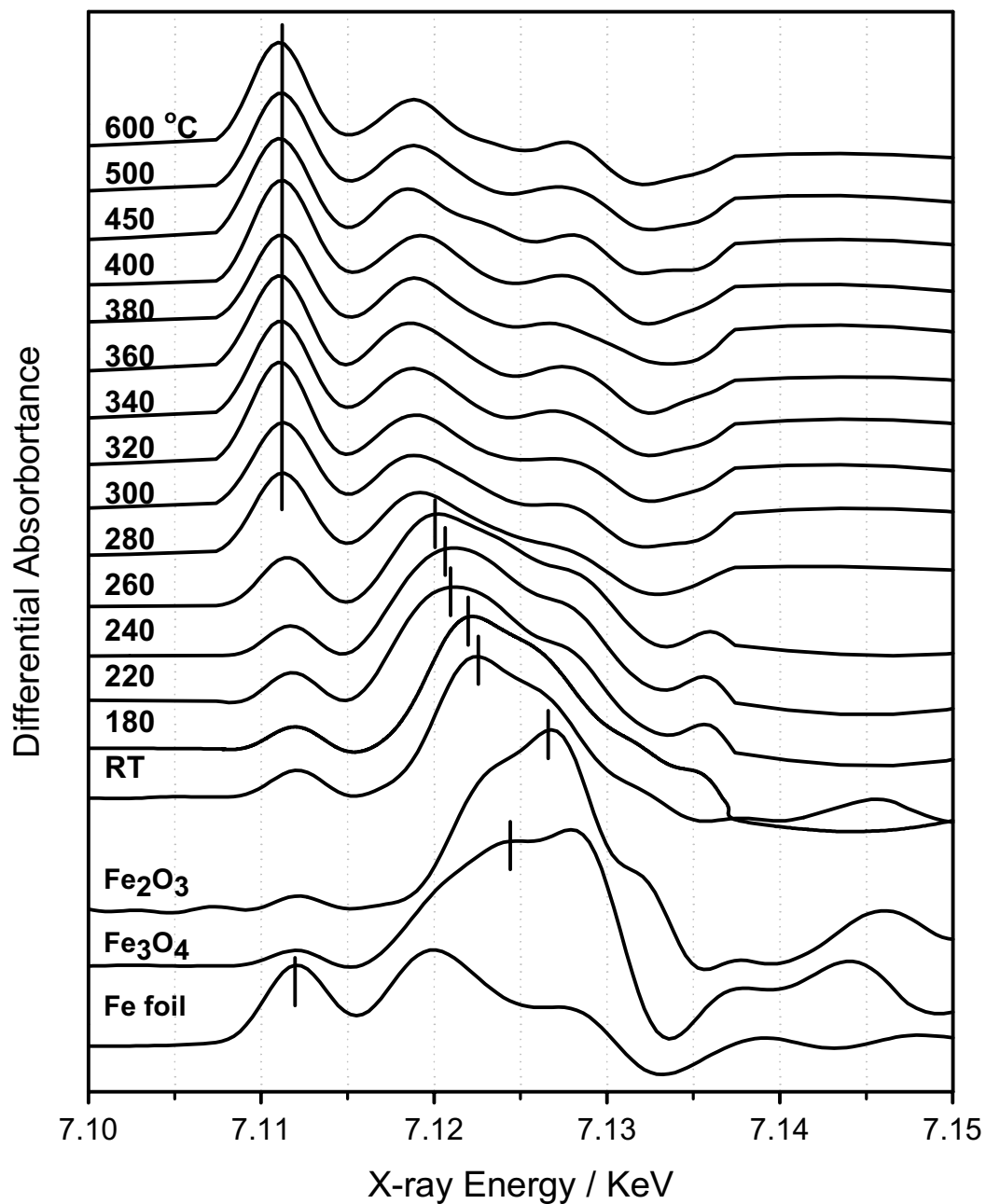
Figure 1.2. Fe K-edge XANES differential spectra of Fe standard compounds: Fe_2O_3, Fe_3O_4 and Fe foil; *In-situ* Fe K-edge XANES differential spectra of a Fe-Zn-K-Cu oxide (Zn/Fe=0.1, K/M=0.02, Cu/M=0.01, M=(Fe+Zn)) in H_2 (8 mg sample; 7 wt.% Fe; 5 cm^3/min H_2) at different temperatures.
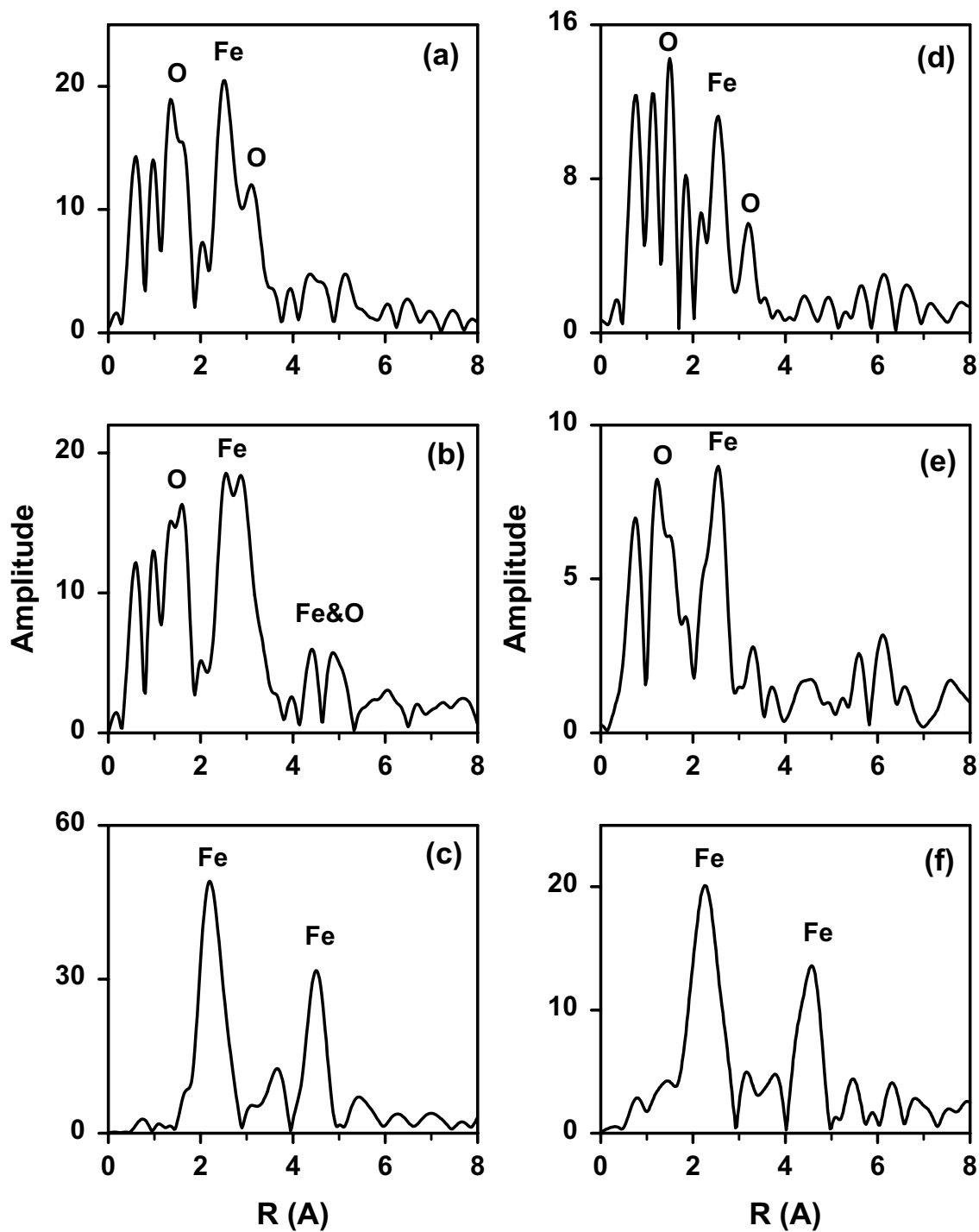
Figure 1.3. EXAFS of Fe K-edge for Fe standard compounds: (a) Fe_2O_3, (b) Fe_3O_4 and (c) Fe foil; *In-situ* EXAFS of Fe-K-edge for a Fe-Zn-K-Cu oxide (Zn/Fe=0.1, K/M=0.02, Cu/M=0.01, M=(Fe+Zn)) in H_2 (8 mg sample; 7 wt.% Fe; 5 cm^3/min H_2) at (d) room temperature, (e) 180 ^{o}C and (f) 600 ^{o}C.

3.3.3. Fe K-Edge EXAFS

Figure 1.3 shows the Fe K-edge EXAFS Fourier transforms of standard compounds Fe_2O_3, Fe_3O_4 and Fe metal, and the Fe-Zn-K-Cu oxide treated in H_2 at 180 ^{o}C and 600 ^{o}C. For Fe_2O_3, Fe is coordinated to first and second closest neighbor oxygen atoms at 1.7 Å and 2.0 Å, respectively; Fe in Fe_3O_4 is coordinated to the first and second closest neighbor oxygen atoms at 1.8 Å and 2.0 Å, respectively. For Fe metal that is body-centered cubic structure, its Fourier transform shows two shells with the first and second closest Fe-Fe distance in the first shell at 2.2 Å and 3.5 Å, respectively. For Fe-Zn-K-Cu oxide, the Fe K-edge Fourier transform resembles that of Fe_2O_3, indicating that it mainly consists of Fe_2O_3. At 180 ^{o}C, some oxygen coordination is lost but Fe is still coordinated with most of oxygen atoms. At 600 ^{o}C, the end of H_2 TPR, the EXAFS spectrum looks like that of Fe metal, indicating the complete reduction of the Fe-Zn-K-Cu oxide to Fe metal.

3.4. In-situ Fe K-edge XAS Measurement for Fe-Zn-K-Cu Oxide in CO

3.4.1. Fe K-Edge XANES

Figure 1.4 shows the Fe K-edge XANES spectra of Fe-Zn-K-Cu oxide in CO at temperatures up to 500 ^{o}C. At 200 ^{o}C, there is no appreciable change of the absorption edge. When increasing the temperature by 100 ^{o}C, both the pre-edge feature and the edge energy change markedly, suggesting significant changes in structures and oxidation states. The pre-edge feature of Fe-Zn-K-Cu oxide disappears and an absorption shoulder similar to that in Fe metal begins to form. When the temperature increases up to 500 ^{o}C, the absorption edge features increasingly resemble those of Fe metal.

3.4.2. Fe K-Edge XANES Differential Spectra

Figure 1.5 shows the Fe K-edge XANES differential spectra of Fe-Zn-K-Cu oxide in CO. Again, the Fe-Zn-K-Cu oxide shows a pre-edge at 7.113 keV. Beyond the pre-edge feature, the spectrum presents the first inflection point at 7.123 keV. There are no evident changes in pre-edge and absorption edges when increasing the temperature up to 200 ^{o}C, indicating that the oxide is not reduced at 200 ^{o}C. After increasing the temperature by 100 ^{o}C, a new inflection point at 7.112 keV emerges as the pre-edge features disappear. This inflection point coincides with that of Fe metal. Since Fe carbides have been confirmed to be the bulk phase at 500 ^{o}C by our previous TPSR experiment, it is believed that this indicates that Fe carbide has the same absorption energy as Fe metal. As the temperature increases to 500 ^{o}C, the edge energy remains at 7.112 keV but the energies of the rest of the inflection points continuously increase or decrease. This suggests that the phase changes continue to occur through the temperature range of the reduction and carburization treatments.

3.4.3. Fe K-Edge EXAFS

Figure 1.6 shows the Fe K-edge EXAFS Fourier transform spectra of Fe-Zn-K-Cu oxide in CO. At 200 ^{o}C, the EXAFS spectra resemble that of its Fe-Zn-K-Cu oxide. At 300 ^{o}C,

the Fe-Fe distance decreases from 2.5 Å in the starting Fe oxide to 2.0 Å, suggesting that a phase transformation occurs. With further carburization, more oxygen atoms are removed. Although a small amount of oxygen remains in the Fe carbide at the end of the carburization (500 $^{\circ}$C), most of the Fe is in the carbide phase. We can conclude that the Fe-Fe distance at 2.0 Å can be ascribed to the Fe-Fe distance in Fe carbides. In addition, it appears that oxygen in Fe-Zn-K-Cu oxide can be removed completely at 500 $^{\circ}$C if enough time or higher temperatures is allowed for carburization.
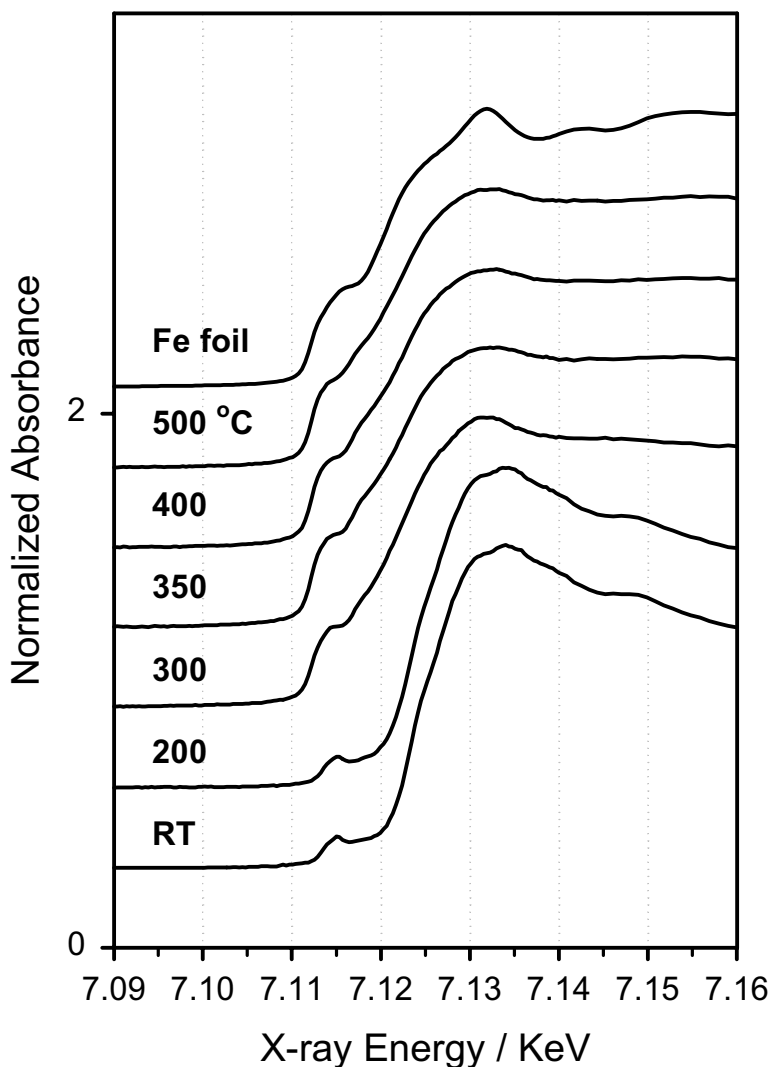

Figure 1.4. *In-situ* Fe K-edge XANES spectra of a Fe-Zn-K-Cu oxide (Zn/Fe=0.1, K/M=0.02, Cu/M=0.01, M=(Fe+Zn)) in CO (8 mg sample; 7 wt.% Fe; 5 cm^3/min CO) at different temperatures.
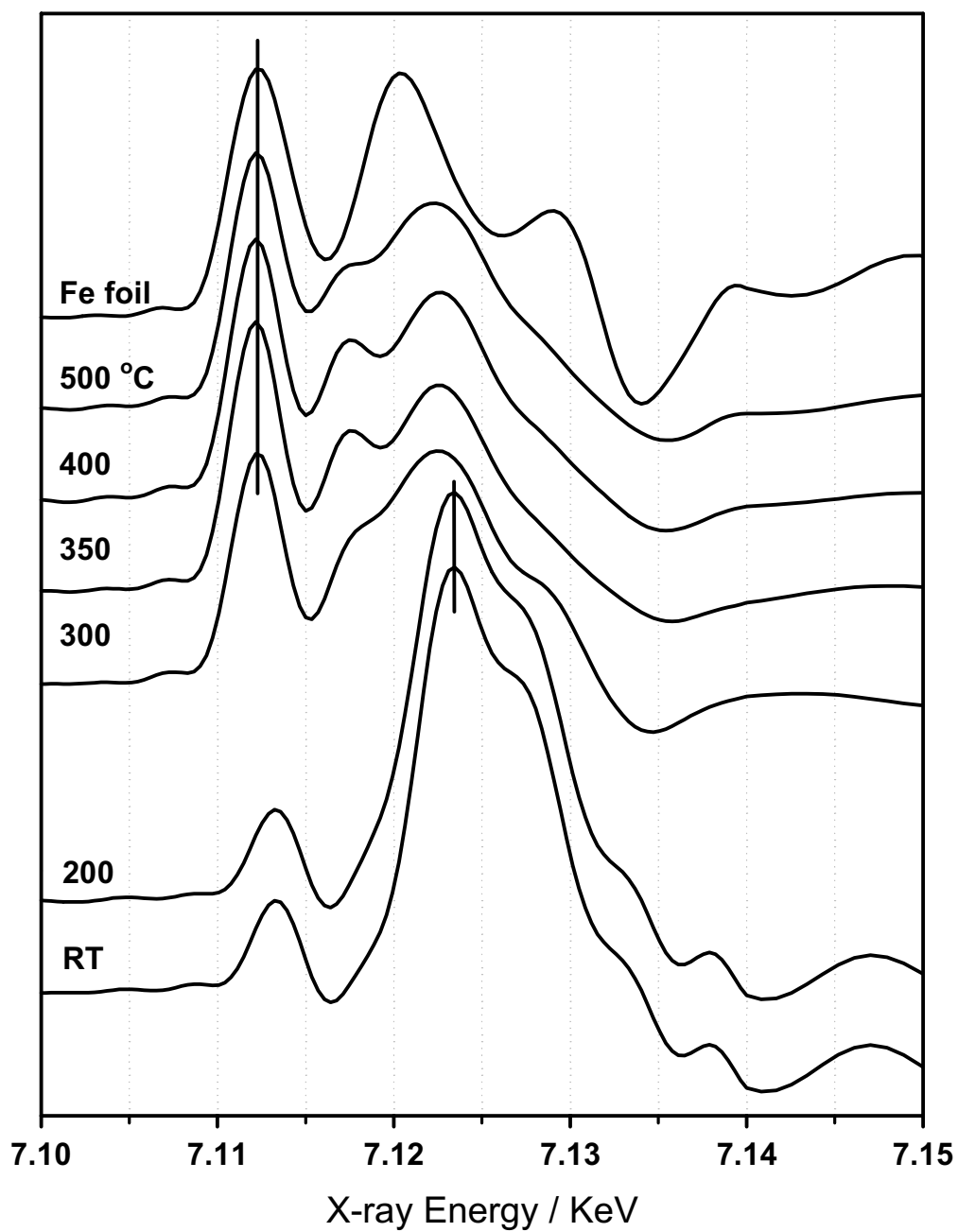
Figure 1.5. *In-situ* Fe K-edge XANES differential spectra of a Fe-Zn-K-Cu oxide (Zn/Fe=0.1, K/M=0.02, Cu/M=0.01, M=(Fe+Zn)) in CO (8 mg sample; 7 wt.% Fe; 5 cm^3/min CO) at different temperatures.
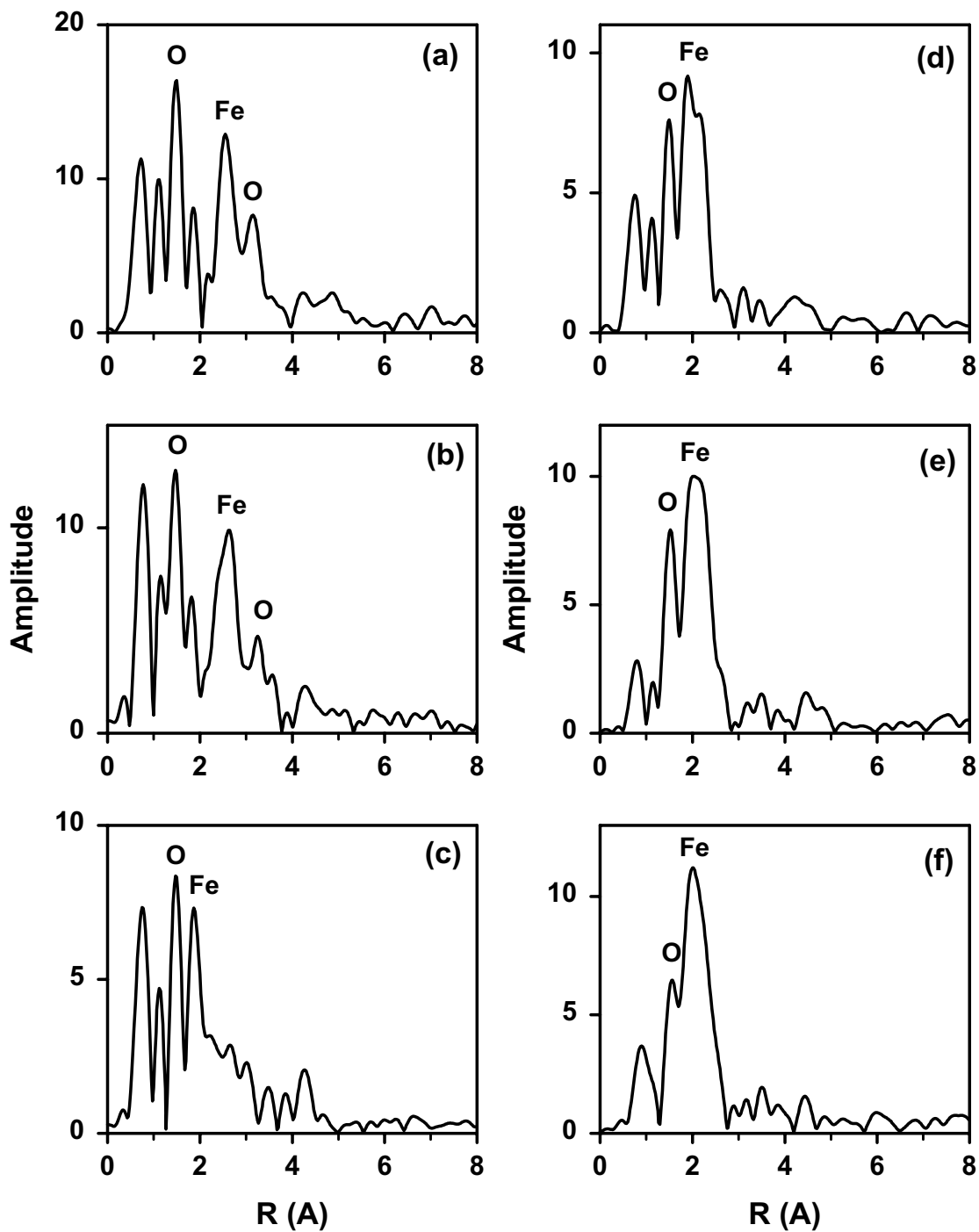
Figure 1.6. *In-situ* Fe-K-edge EXAFS for Fe-Zn-K-Cu oxide (Zn/Fe=0.1, K/M=0.02, Cu/M=0.01, M=(Fe+Zn)) in CO (8 mg sample; 7 wt.% Fe; 5 cm^3/min CO) at (a) RT, (b) 200 ^{o}C, (c) 300 ^{o}C, (d) 350 ^{o}C, (e) 400 ^{o}C, (f) 500 ^{o}C.

3.5.   In-situ Fe K-edge XAS Measurement for Fe-Zn-K-Cu Oxide in Synthesis Gas

3.5.1.   Fe K-Edge XANES

Figure 1.7 shows the Fe K-edge XANES spectra of Fe-Zn-K-Cu oxide in synthesis gas at 270 ^{o}C with varying space velocities. With increasing space velocity, we observed minor changes of the pre-edge features and the slight shifts of the absorption edges to lower energies. However, the global features resemble Fe-Zn-K-Cu oxide more than Fe metal.

3.5.2   Fe K-Edge XANES Differential Spectra

Figure 1.8 shows the Fe K-edge XANES differential spectra of the Fe-Zn-K-Cu oxide in synthesis gas with varying space velocities. At 200 ^{o}C, the absorption edge moves to lower energies in synthesis gas than in CO at the same temperature (Figure 1.5). This confirms our TPSR conclusion that reduction occurs at lower temperatures in H_2 than in CO, because H_2 dissociates on the reduced Cu at lower temperatures and consequently decreases the required reduction temperature. With increasing temperature up to 270 ^{o}C and with increasing space velocity, the absorption edge shifts slightly to lower energies and the peak at the pre-edge region increases and shifts slightly to lower energy regions. This shift and the increase of the peak at the pre-edge region indicate the formation of a new phase Fe carbide with an absorption edge energy at 7.112 keV.

3.5.3.   Fe K-Edge EXAFS

Figure 1.9 shows the Fe K-edge EXAFS Fourier transform spectra of Fe-Zn-K-Cu oxide in synthesis gas. The Fe K-edge EXAFS in synthesis gas is more complicated than in CO or H_2. Although Fe is mainly coordinated to oxygen atoms, a peak at a radius of 2.0 Å begins to form, which represents the Fe-Fe distance in Fe carbide. This peak increases with increasing space velocity and with time on stream. This indicates that Fe carbide is formed, although the dominant bulk phase remains Fe oxide. When the temperature is decreased to 250 ^{o}C, Fe oxides continue to carburize. This suggests that the extent of carburization increase with increasing space velocity and with time on stream.

3.6.   Potassium K-Edge XANES of Fe-Zn-K-Cu Oxides and Carbides

Figure 1.10 shows the potassium K-edge XANES spectra of K_2CO_3 and of several Fe oxide samples with varying K contents. The XANES spectra of K_2CO_3 are dominated by two major peaks: the first peak at ~ 3 eV represents the transition of $1s$ electrons to continuum, whereas the second peak with X-ray energy at 10 eV is the result of multiple scattering resonances. For K-promoted Fe oxides with different Zn contents (Fig 1.10 (a), (b), (d)), the post-edge features of the samples are significantly different from that in K_2CO_3. Although we need to examine other standard K compounds in order to identify the phases of K in these Fe catalysts, it is clear that K is not present as bulk K_2CO_3 crystallites. Rather, K is well dispersed on Fe and Zn oxides. After carburization in CO up to 800 ^{o}C (Fig1.10 (c)), the carbide samples have more characteristic post-edge features of K_2CO_3, and the higher the K and Cu contents, the more likely K is the form of

K_2CO_3. It appears that the bonding between K and Fe or Zn is broken during carburization, and K recombines forming K_2CO_3 in Fe carbides.
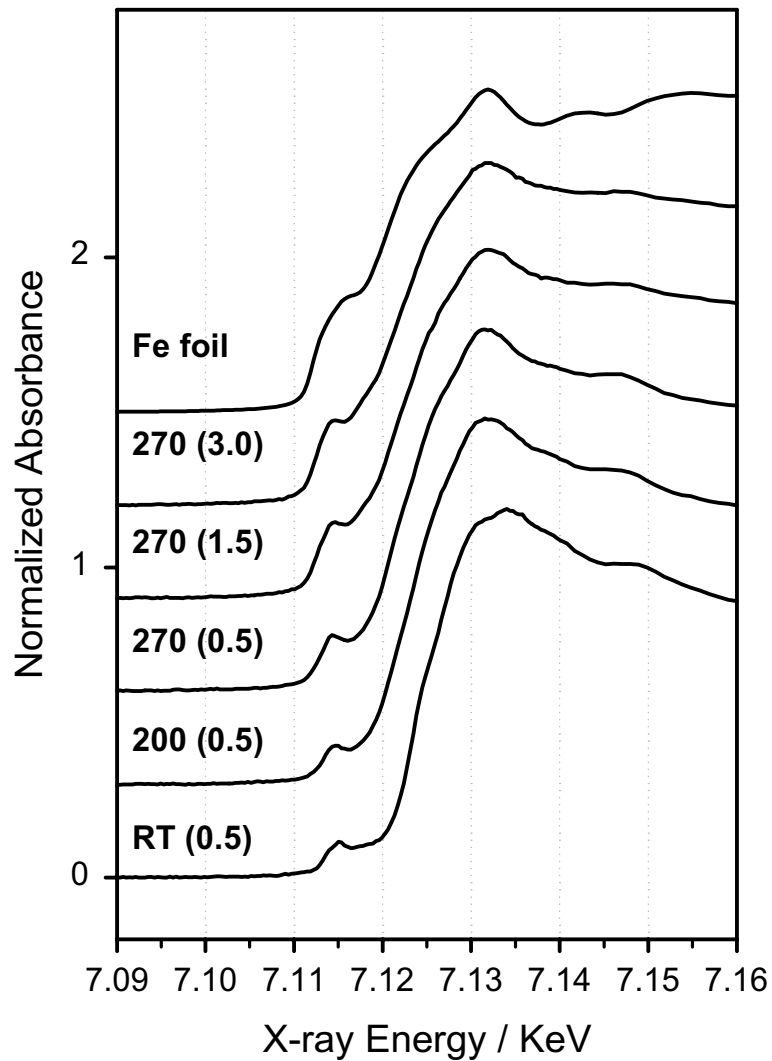

Figure 1.7. *In-situ* Fe K-edge XANES spectra of a Fe-Zn-K-Cu oxide (Zn/Fe=0.1, K/M=0.02, Cu/M=0.01, M=(Fe+Zn)) in CO/H_2 (8 mg sample; 7 wt% Fe; CO/H_2=1/2, 0.5-3 cm^3/min) at different temperatures and space velocities.
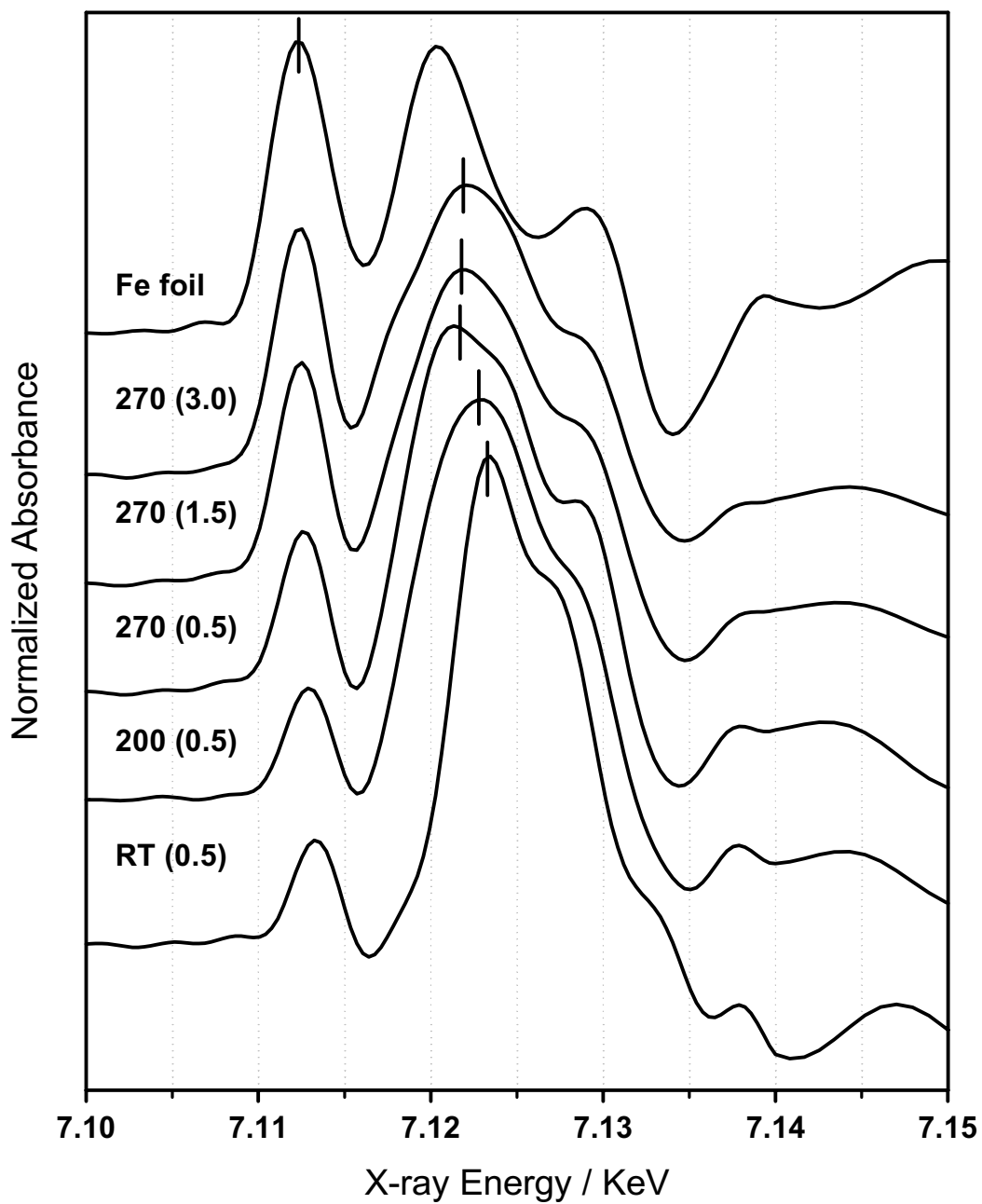
Figure 1.8. *In-situ* Fe K-edge XANES differential spectra of a Fe-Zn-K-Cu oxide (Zn/Fe=0.1, K/M=0.02, Cu/M=0.01, M=(Fe+Zn)) in CO/H_2 (8 mg sample; 7 wt% Fe; CO/H_2=1/2, 0.5-3 cm^3/min) at different temperatures and space velocities.
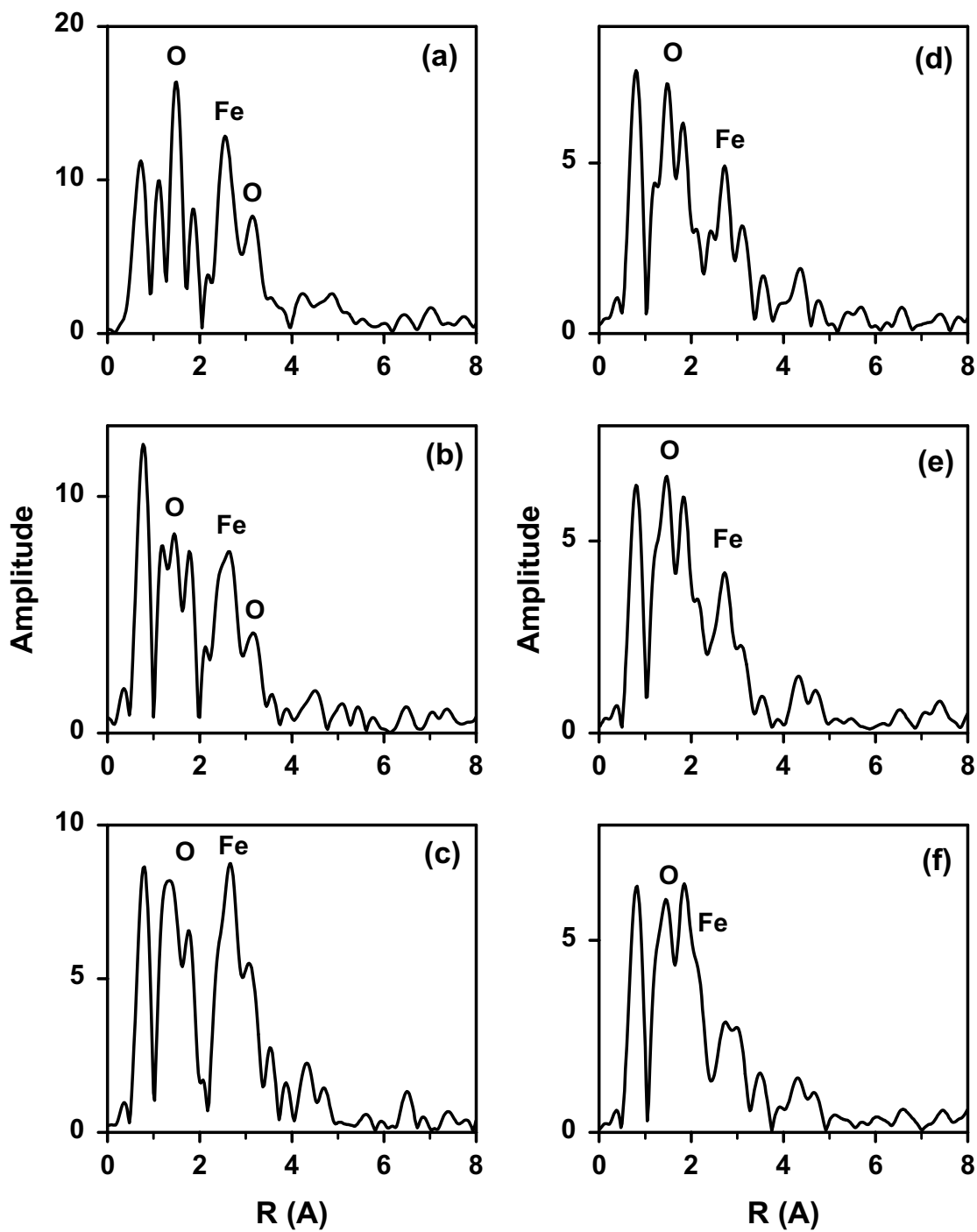
Figure 1.9. *In-situ* Fe K-edge EXAFS spectra for a Fe-Zn-K-Cu oxide (Zn/Fe=0.1, K/M=0.02, Cu/M=0.01, M=(Fe+Zn)) in CO/H_2 (8 mg sample; 7 wt% Fe; CO/H_2=1/2, 0.5-3 cm^3/min) at (a) RT (0.5 cm^3/min), (b) 200 $^{\circ}$C (0.5 cm^3/min), (c) 270 $^{\circ}$C (0.5 cm^3/min), (d) 270 $^{\circ}$C (1.5 cm^3/min), (e) 270 $^{\circ}$C (3 cm^3/min), (f) 250 $^{\circ}$C (3 cm^3/min).
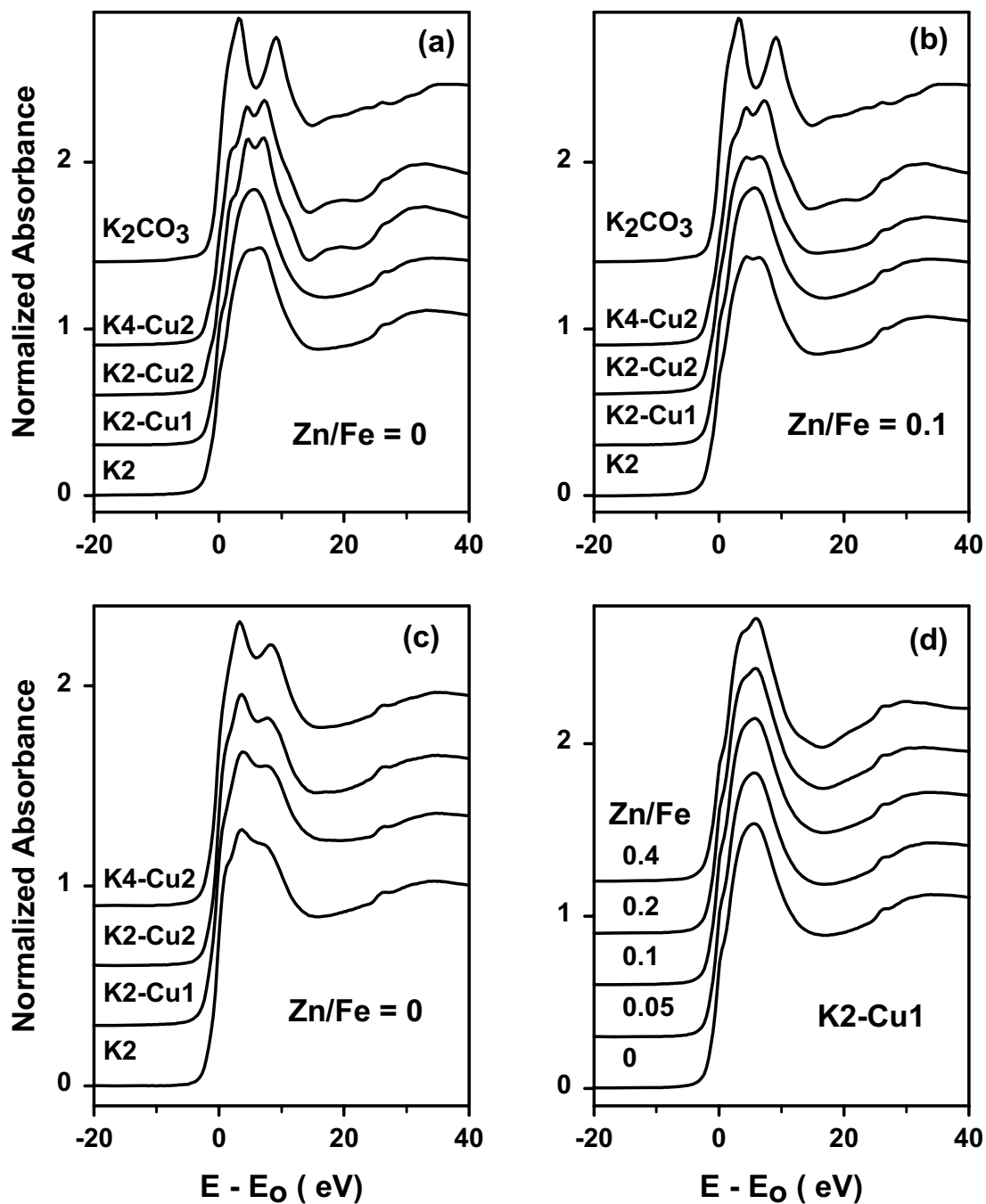
Figure 1.10. Potassium K-edge XANES spectra of K_2CO_3 and K-promoted Fe oxides. (a) Zn/Fe=0, K/M=0.02-0.04; (b) Zn/Fe=0.1, K/M=0.02-0.04; (c) Zn/Fe=0, K/M=0.02-0.04 after carburization in CO up to 800 ^{o}C (0.2 g sample; 10 ^{o}C ramping rate; 100 cm^3/min, 20% CO in Ar); (d) K/M=0.02, Zn/Fe=0-0.4, and M=(Zn+Fe).

4.   Fischer-Tropsch synthesis on Fe-based catalysts

4.1.   *Investigation of K Effects on FTS Reactions*

In the last quarter, we reported partial results about K effects on the catalytic activities for both the Fischer-Tropsch synthesis (FTS) and the concurrent water-gas shift (WGS) reactions and hydrocarbon selectivities on Fe-based catalysts. Experiments and data analyses on K promotion effects were completed during this reporting period. We report here K effects on secondary reactions (hydrogenation and isomerization) of primary α-olefin products on Fe-based catalysts (Zn/Fe=0.1, Cu/M=0.0.1) with varying K contents (K/M=0-0.04) in a fixed-bed reactor at different temperatures and pressures (235 ^{o}C and 21.4 atm; 270 ^{o}C and 5 atm) using synthesis gas with a H_2/CO ratio of 2:1. Some preliminary versions of the data presented here were initially reported last quarter.

4.1.1   Effects of K on the Secondary Hydrogenation of α-Olefins

During the FTS reaction, chains terminate either by β-hydrogen abstraction to form α-olefins or by H-addition to form paraffins. The primary α-olefin products undergo secondary hydrogenation reactions to form n-paraffins [16]. The linear α-olefins can potentially be used for the manufacture of high-value chemicals. For example, the C_6-C_{16} linear α-olefins are used for the manufacture of biodegradable detergents and PVC plasticizers. Thus, from the viewpoint of producing chemicals and chemical feedstocks, FTS catalysts should have a high selectivity to linear α-olefins. The addition of K has been reported to inhibit secondary reactions of primary α-olefins, increasing their selectivities [19].

Fig. 1.11 shows the propene/propane ratio as a function of CO conversion on the catalyst with varying K loading at 235 ^{o}C and 21.4 atm. We use the propene/propane ratio as a measure of secondary olefin hydrogenation activity because of the high selectivity to C_3 and the high hydrogenation reactivity of propene (only lower than ethylene). The results show that these ratios are almost independent of CO conversion on K-promoted catalysts, suggesting that secondary hydrogenation reactions of propene are not present and the ratio is only determined by the relative probability of chain termination to propane and to propene. In contrast, propene/propane ratio decreases with increasing CO conversion on the K-free catalyst. This result indicates the presence of secondary hydrogenation of propene. The ratio was also plotted against propene residence time (e.g. space time), as shown in Fig. 1.12, which seems that the propene/propane ratio decreases with propene residence time, confirming that some propene was hydrogenated to form propane on the K-free catalyst.   It is well known that acid sites catalyze olefin hydrogenation. Potassium, an alkaline metal, may titrate acid sites. Therefore, the K-promoted catalysts may lose the activity for hydrogenation at 235 ^{o}C.
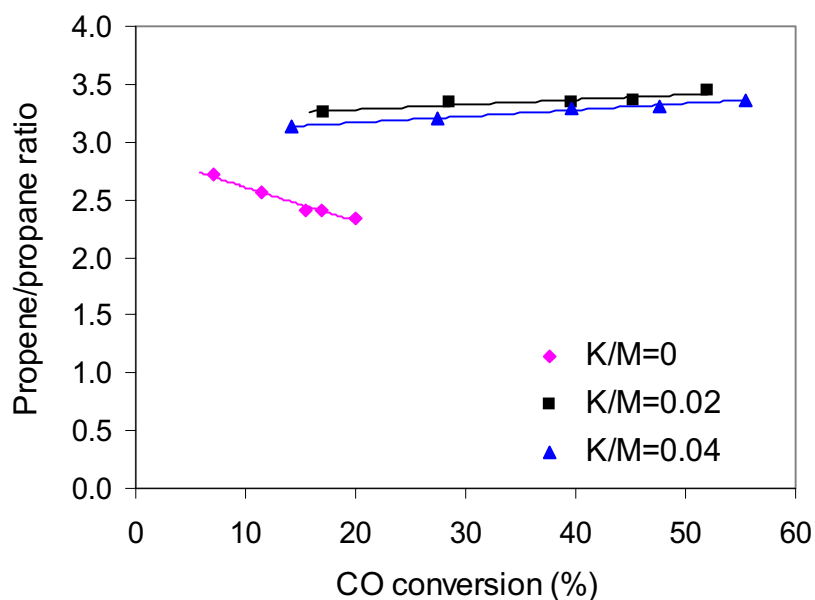
Fig. 1.11. Propene/propane ratio as a function of CO conversion on the (Zn/Fe=0.1, Cu/M=0.01) with various K loadings (K/M=0-0.04) at 235 ^{o}C and 21.4 atm, H$_2$/CO=2.

Fig. 1.12. Propene/propane ratio as a function of propene space time on the catalyst (Zn/Fe=0.1, Cu/M=0.01) with varying K loading (K/M=0-0.04) at 235 ^{o}C and 21.4 atm, H$_2$/CO=2.

Propene/propane ratios decreased with propene residence times at 270 ^{o}C and 5 atm on K-free and K-promoted catalysts (Fig. 1.13). The K-promoted catalysts now show secondary hydrogenation reactions of propene due to the increase of temperature.
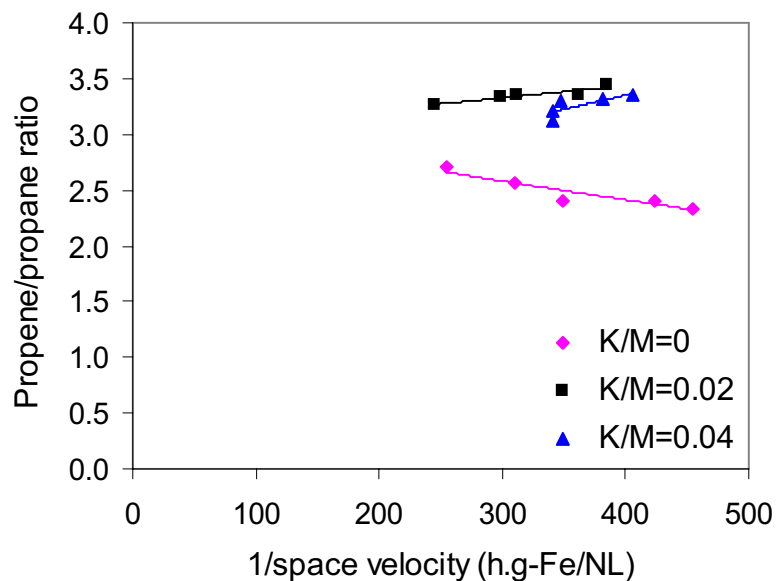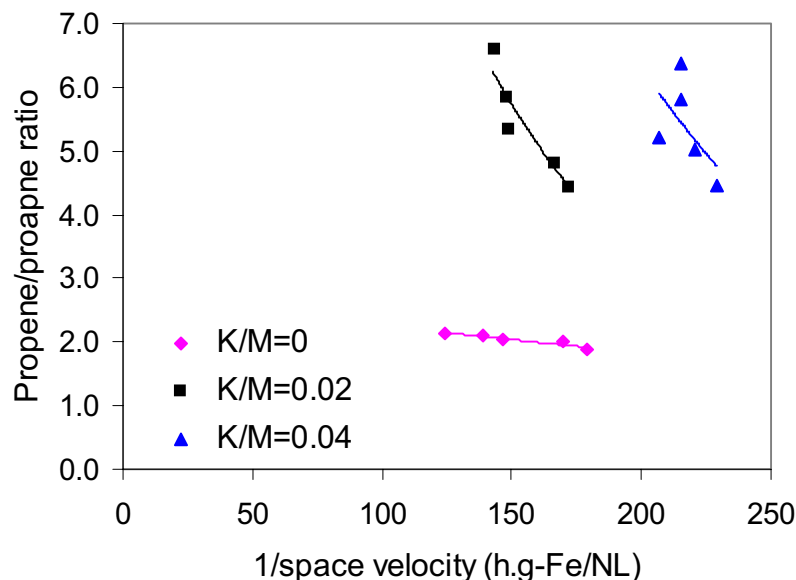

Fig. 1.13. Propene/propane ratio as a function of propene space time on the catalyst (Zn/Fe=0.1, Cu/M=0.01) with varying K loading (K/M=0-0.04) at 270 ^{o}C and 5 atm, H$_2$/CO=2.

4.1.2. Effects of K on the Secondary Isomerization of α-Olefins

The primary α-olefins produced by β-hydrogen abstraction during the FTS reaction undergo secondary hydrogenation reaction to form n-paraffins, as discussed previously. Similarly, the primary α-olefins may also undergo secondary isomerization reactions to produce internal or branched olefins [16]. The molar fraction of all internal and branched olefin isomers in total olefins represents the extent of isomerization of the primary α-olefins. In this report, we refer all internal and branched butene isomers as butene isomers.

The molar fraction of butene isomers as a function of CO conversion over all catalysts at 235 ^{o}C and 21.4 atm is shown in Fig. 1.14. The results show butene isomer molar fraction on K-free catalyst is much higher than the fraction on K-promoted catalysts. It is well known that acid catalysts are active for olefin isomerization. Therefore, it is expected that butene isomer molar fraction declines when K is introduced to the catalyst.

The molar fraction of butene isomers increased with CO conversion on the K-free catalyst. Assuming that all butene isomers were formed from primary α-butene, the residence time of primary α-butene can be calculated. The residence times of the primary α-butene on the three catalysts as a function of CO conversion are plotted in Fig. 1.15. Since these residence times of the primary α-butene increase with increasing CO

conversion, it is natural that the conversion of primary α-butene (e.g. isomerization) increases with CO conversion on the K-free catalyst.
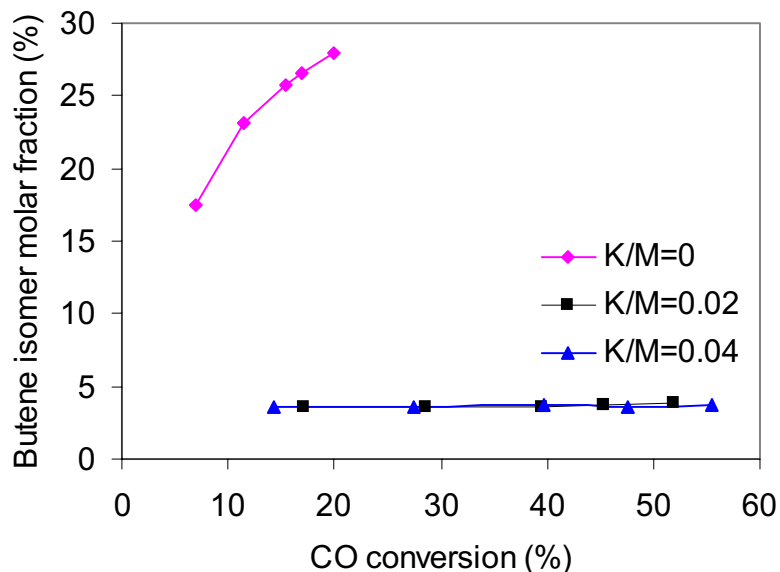

Fig. 1.14. The molar fraction of butene isomers as a function of CO conversion on the catalysts (Zn/Fe=0.1, Cu/M=0.01) with various K loading levels (K/M=0-0.04) at 235 $^{\circ}$C and 21.4 atm, H_2/CO=2.
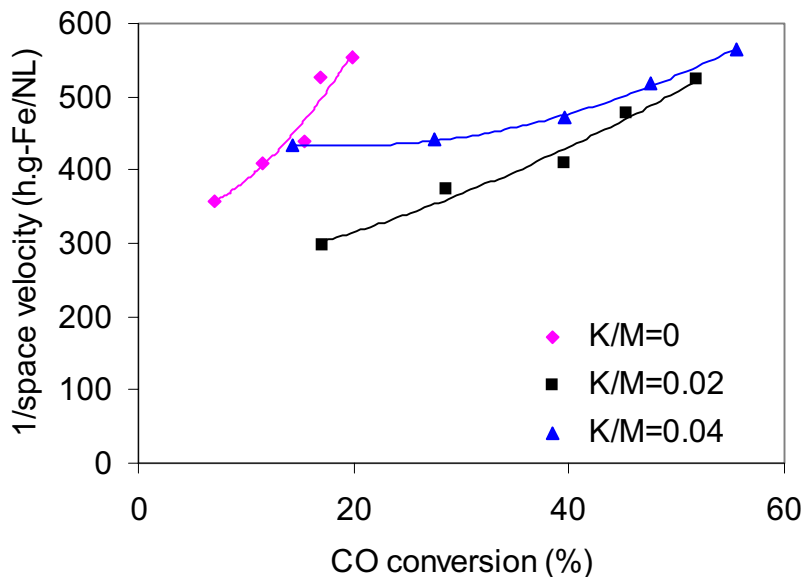

Fig. 1.15. The space time of α-butene as a function of CO conversion on the catalysts (Zn/Fe=0.1, Cu/M=0.01) with various K loading levels (K/M=0-0.04) at 235 $^{\circ}$C and 21.4 atm, H_2/CO=2.

However, the molar fractions on K-promoted catalysts are almost independent of CO conversion, suggesting that the butene isomers may not be formed from primary α-butene. If the butene isomers were formed from primary α-butene, the conversion of primary α-butene (isomerization) should increase with its residence time. This is inconsistent with our observations (Figs. 1.14 and 1.15). Hence, it can be concluded that the K-promoted catalyst has no activity for secondary isomerization of primary olefins and the olefin isomers are primary products during the FTS at 235 ^{o}C and 21.4 atm.

Fig. 1.16 shows the molar fractions of butene isomers as a function of CO conversion on all three catalysts at 270 ^{o}C and 5 atm. More than half of the butenes consists of internal butenes on the K-free catalyst at 270 ^{o}C, indicating that the K-free catalyst is very active for isomerization of olefins at high temperature. The molar fraction of butene isomers at 270 ^{o}C is higher than that at 235 ^{o}C, and increases with increasing CO conversion on K-promoted catalysts. These results suggest that at the higher temperature, the K-promoted catalysts become active for isomerization of primary α-butene. Since some butene isomers are formed from the primary α-butene, the molar fraction of butene isomers is expected to increase with increasing CO conversion because the residence time of the primary α-butene increases with CO conversion.
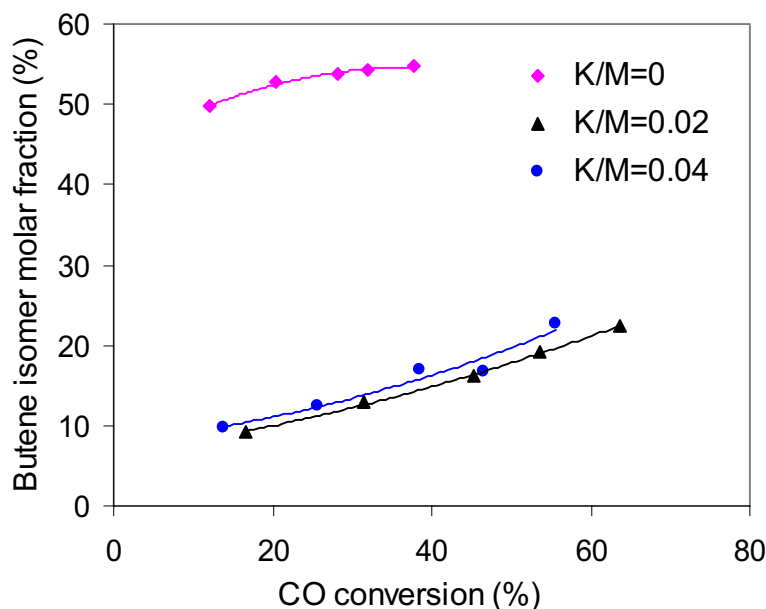

Fig. 1.16. The molar fraction of butene isomers as a function of CO conversion on the catalysts (Zn/Fe=0.1, Cu/M=0.01) with various K loading levels (K/M=0-0.04) at 270 ^{o}C and 5 atm, H$_2$/CO=2.

The molar fraction of butene isomers is higher on the catalyst with higher K loading than that with an intermediate K loading at the same CO conversion at 270 ^{o}C. This can misleadingly suggest that the catalyst with higher K loading is more active for isomerization at 270 ^{o}C. When the conversion of the primary α-butene was plotted against its residence time (Fig. 1.17), the data indicated that the opposite conclusion could be reached. The conversion of primary α-butene was calculated by assuming that

no other products besides butene isomers were formed from primary α-butene. Coincidentally, this conversion is equal in value to the molar fraction of butene isomers. It is clearly shown that the conversion of primary α-butene is higher on the catalyst with an intermediate K loading at the same residence time. Hence, this catalyst is more active for α-butene isomerization.
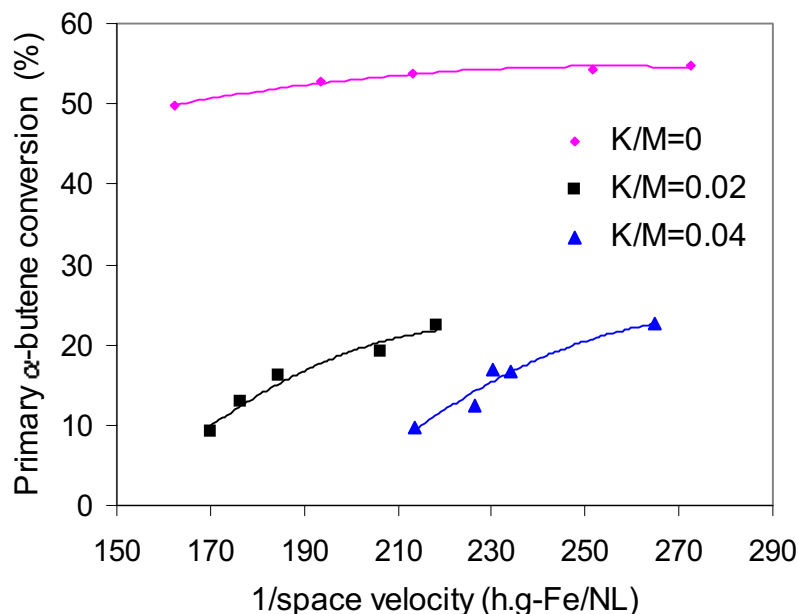

Fig. 1.17. The conversion of the primary α-butene as a function of the residence time of the primary α-butene on the catalysts (Zn/Fe=0.1, Cu/M=0.01) with various K loading levels (K/M=0-0.04) at 270 ^{o}C and 5 atm, H$_2$/CO=2.

In summary, Fe-Zn-Cu catalysts are active for secondary hydrogenation and isomerization reactions of α-olefins. The introduction of K to these catalysts can titrate their active sites. At 235 ^{o}C, the K-promoted catalysts show no activity for secondary reactions. At 270 ^{o}C, these K-promoted catalysts become active for secondary reaction but their activities are much lower than that of the K-free catalyst.

4.2. *Investigation of Cu Effects on FTS Reactions*

Copper has been widely used as one of the promoters on iron catalysts. Its function is to decrease the temperature required for the reduction and carburization of iron oxides [16, 21]. A synergistic effect between K and Cu was previously reported for FTS catalysts based on Fe-Zn oxides [21]. In this reporting period, we began a study of the promotion effects of Cu on FTS. We focused on the catalysts (Ze/Fe=0.1, K/M=0.02) with various Cu loading (Cu/M=0-0.02). The results at 235 ^{o}C and 21.4 atm are reported here.

4.2.1 Effects of Cu on the FTS and the WGS Activities

CO conversion for various Cu loading (Cu/M=0-0.02) studied at 235 ^{o}C and 21.4 atm is shown in Fig. 1.18. The Cu-free catalyst showed lower FTS rates. At the same space velocity, higher CO conversion was obtained on Cu-promoted catalysts. However, the catalyst with a higher Cu loading (Cu/M=0.02) did not exhibit a greater activity than the catalyst with an intermediate Cu loading (Cu/M=0.01). These results are in agreement with previous reports [16,21-22]. Kolbel *et al.* [22] observed an increase in the overall activity already at a very low Cu content (ca. 0.1 wt.% Cu), and further increases in Cu content had no additional effect. The reasons for the increased activity with the addition of Cu are not clearly understood. It is known that Cu facilitates reduction of iron and that the total surface area of the catalyst decreases with the extent of metal reduction [1]. This suggests that the higher activity of Cu-promoted catalysts to Cu-free catalysts may be attributed to the differences in the size and number of iron carbide crystallites during synthesis [21].
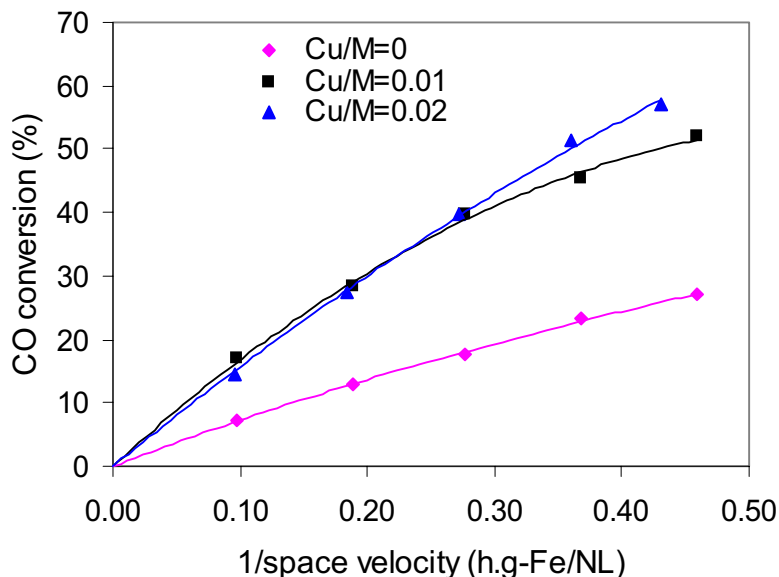

Fig. 1.18. CO conversion as a function of reciprocal space velocity on the catalysts (Zn/Fe=0.1, K/M=0.02) with various Cu loading levels (Cu/M=0-0.02) at 235 ^{o}C and 21.4 atm, H_2/CO=2.

During FTS, water is the primary oxygenate product, and CO_2 forms via a subsequent water-gas shift. Higher CO_2 selectivity means that more CO_2 is produced from water and CO, i.e., the catalyst is more active for water-gas shift reactions. Fig. 1.19 shows CO_2 selectivity as a function of CO conversion with varing Cu loading at 235 ^{o}C and 21.4 atm. CO_2 selectivity increased with CO conversion at all Cu loading. This is expected if more water is produced at the higher CO conversion. CO_2 selectivity was considerably increased after Cu was introduced into the catalyst. The increase in CO_2 selectivity with Cu is expected since Cu is a well-known low-temperature WGS catalyst. Additional

effects on CO_2 selectivity with higher Cu loading (Cu/M=0.02) were not observed. The promotion effect of Cu is smaller than that of K on WGS reaction, as shown in Fig. 1.20.
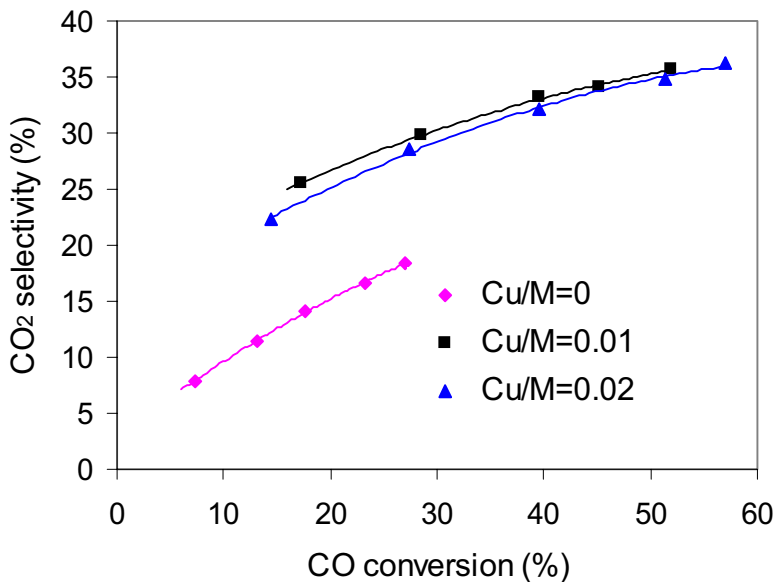

Fig. 1.19. CO_2 selectivity as a function of CO conversion on the catalysts (Zn/Fe=0.1, K/M=0.02) with various Cu loading levels (Cu/M=0-0.02) at 235 ^{o}C and 21.4 atm, H_2/CO=2.
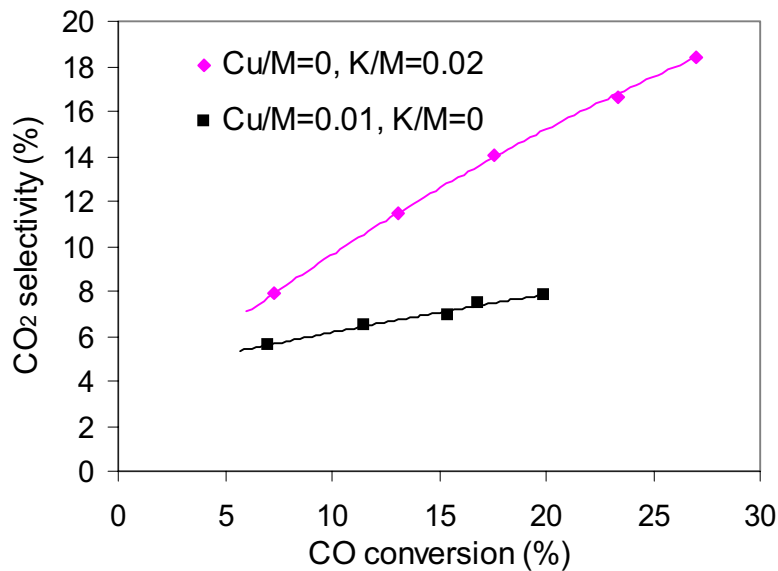

Fig. 1.20. CO2 selectivity as a function of CO conversion on the K-promoted catalyst (Zn/Fe=0.1, K/M=0.02, Cu/M=0) and the Cu-promoted catalyst (Zn/Fe=0.1, K/M=0, Cu/M=0.01) at 235 ^{o}C and 21.4 atm, H_2/CO=2.

4.2.2. Effects of Cu on Hydrocarbon Selectivity and α-Olefin to n-Paraffin Ratio

Figs. 1.21-23 show methane and C_{5+} selectivities and α-olefin/n-paraffin ratios as a function of CO conversion on the catalysts (Zn/Fe=0.1, K/M=0.1) with varying Cu loading (Cu/M=0-0.02) at 235 ^{o}C and 21.4 atm. The promotion effects of Cu on the hydrocarbon and olefin selectivities are much less marked than those observed for K.
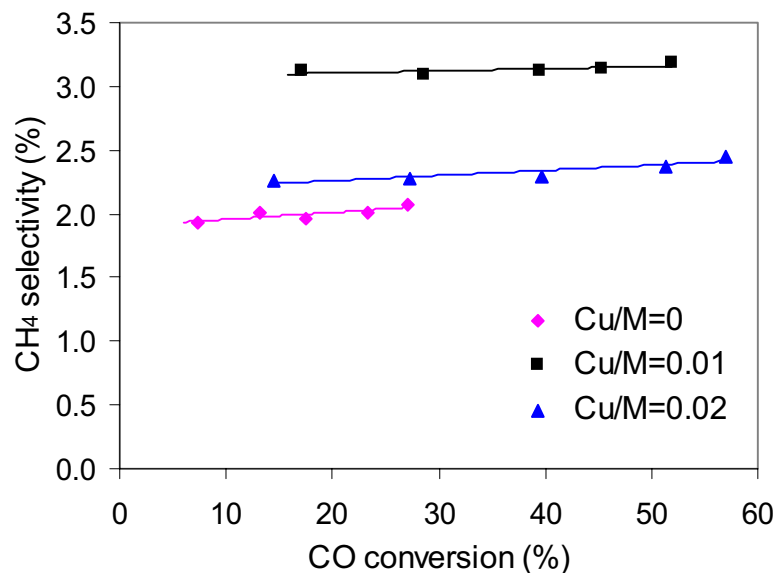

Fig. 1.21. Methane selectivity as a function of CO conversion on the catalysts (Zn/Fe=0.1, K/M=0.02) with various Cu loading levels (Cu/M=0-0.02) at 235 ^{o}C and 21.4 atm, $H_2/CO=2$.
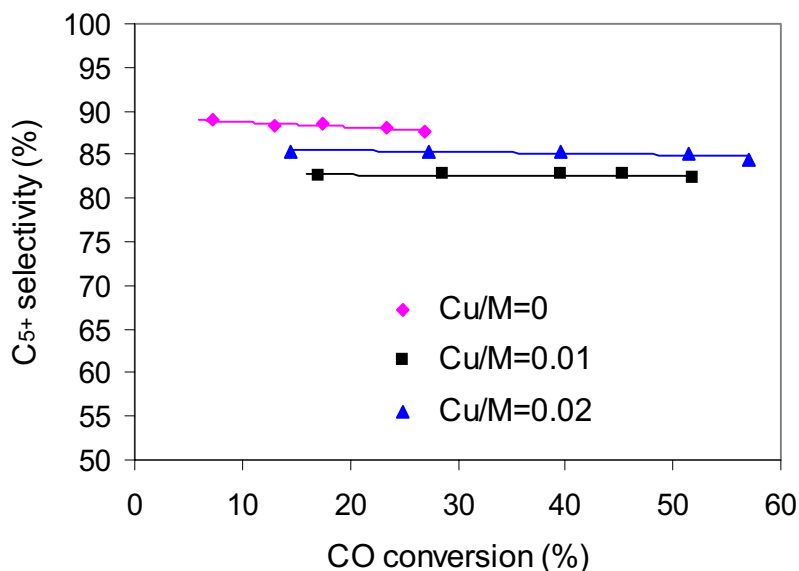

Fig. 1.22. C_{5+} selectivity as a function of CO conversion on the catalysts (Zn/Fe=0.1, K/M=0.02) with various Cu loading levels (Cu/M=0-0.02) at 235 ^{o}C and 21.4 atm, $H_2/CO=2$.

74
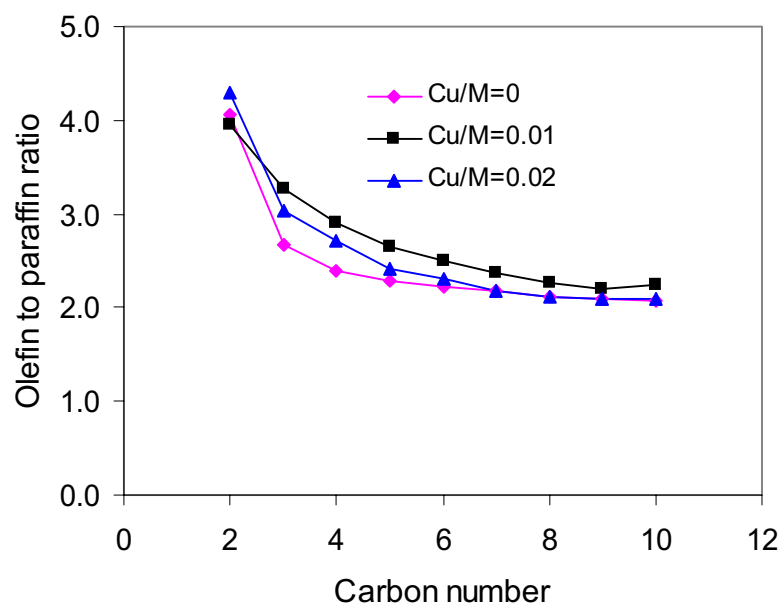
Fig. 1.23. α-Olefin to n-paraffin ratio as a function of CO conversion on the catalysts (Zn/Fe=0.1, K/M=0.02) with various Cu loading levels (Cu/M=0-0.02) at 235 ^{o}C and 21.4 atm, H_2/CO=2, CO conversion ~15%.

4.3.   *Synergistic Effects of Cu and K on FTS Reactions*

As we discussed above, the addition of K has a larger effect than the addition of Cu on hydrocarbon and olefin selectivities. Both K and Cu, however, improve the activity of Fe-Zn catalysts.
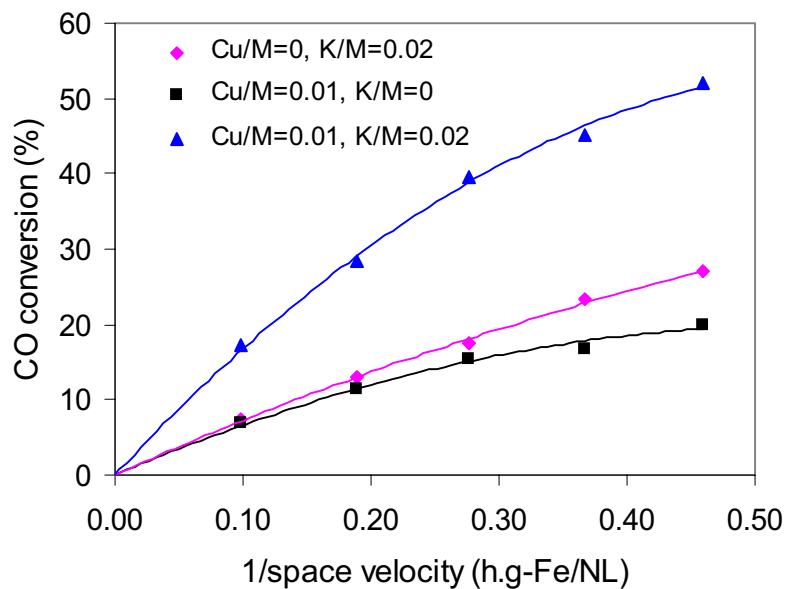
Fig. 1.18. CO conversion as a function of reciprocal space velocity on the singly and doubly promoted catalysts (Zn/Fe=0.1) at 235 ^{o}C and 21.4 atm, H_2/CO=2.

75

Fig. 1.24 shows CO conversion as a function of space time for two individually (K or Cu) promoted catalysts and doubly promoted catalyst. It is seen that simultaneous promotion of Fe-Zn with K and Cu leads to higher activity than the individually promoted catalysts, suggesting the synergistic effects of K and Cu. Soled *et al*. observed the same effect for the FTS in slurry reactor [16]. They observed that the catalyst promoted with only K or Cu had little effect on CO conversion, compared to the unpromoted Fe-Zn catalyst, while doubly promoted catalyst increased CO conversion from ~ 40 % to 73 %.

II.   FISCHER-TROPSCH SYNTHESIS ON COBALT CATALYSTS

1.   Background

We showed in the previous quarterly report that water, a reaction product of FTS, not only influences the reaction selectivity but also enhances the rate of primary CO hydrogenation on cobalt catalysts. The positive water effect on the synthesis rate has been observed by other investigators [23,24]. However, this subject is still controversial since water was also found to have no significant effect on CO consumption rate in some other studies [25,26]. So far, kinetic rate equations reported in literature for FTS with cobalt catalysts do not account for these water effects. During this reporting period, the reaction kinetics of FTS were studied on a Co/SiO_2 catalyst over a wide range of reaction pressures and $H_2/CO/H_2O$ ratios. The D_2-H_2 exchange experiment was performed under FTS conditions in an attempt to examine the reversibility of hydrogen adsorption. Subsequently, a reaction mechanism for the cobalt-catalyzed FTS was proposed. Using this mechanism and applying the pseudo-steady state approximation (PSSA) the mechanism, a kinetic rate expression based on Langmuir-Hinshelwood model was obtained.

2.   Experimental

Fischer-Tropsch synthesis kinetics was studied using a fixed-bed, single-pass flow reactor. The reactants, H_2 (Matheson, UHP) and CO/N_2 (Matheson, UHP, 81.5/18.5, molar ratio) were introduced into the reactor separately using mass flow controllers (Brooks, model 5850). The cobalt catalyst used was a 21.9 wt.% Co/SiO_2 catalyst. The preparation and pretreatment of the cobalt catalyst were described in the previous quarterly report. The reactor was kept at 20 atm, 200°C and $H_2/CO = 2.0$ for the first 100 h in order to allow the catalyst to achieve steady-state operation. For the kinetic studies, reactor pressures were changed from 13 to 33 atm and H_2/CO feed ratios from 1.3 to 8.5. The conversion of CO was varied from 5 to 30% by changing the space velocity. When the reaction conditions were changed, a period of at least 12 h was allowed between balance periods. N_2 (used as an internal standard), CO, CO_2, and light hydrocarbons (C_1-C_{12}) were analyzed by on-line gas chromatography (Hewlett-Packard 5890) using thermal conductivity and flame ionization detections. Synthesis rate was reported as a site-time yield (molar CO converted per g atom surface Co).

Isotopic exchange between H_2 and D_2 was carried out during FTS (200°C, 20 atm). The reactants, H_2 (Matheson, UHP), D_2 (Cambridge Isotope Laboratories, Inc., 99.8%), and CO/N_2 (Matheson, UHP, 81.5/18.5) were introduced into the reactor separately using mass flow controllers (Brooks, model 5850) at a molar ratio of $H_2/D_2/CO/N_2$ = 31/31/31/7. The deuterium fraction in hydrogen isotopomers was determined by off-line mass spectrometry (Leybod Inficon Instruments Co., Inc.). A blank run of D_2-H_2 exchange was also carried out with the SiO_2 diluent.

3.   FTS on Cobalt-Based Catalysts

3.1 D_2-H_2 Exchange and D_2O Tracer

D_2-H_2 exchange was carried out during FTS (200°C, 20 atm). The formation rate of the HD was compared to the rate of hydrogen converted to hydrocarbons (Figure 2.1). The isotopic exchange rates presented here have been calibrated by subtracting those measured in a blank run using SiO_2. The hydrogen exchange rate decreased from 450 h^{-1} to 200 h^{-1} as the CO conversion increased from 6% to 15% (by decreasing bed residence time), while the rates of hydrogen conversion to hydrocarbons were less than 50 h^{-1}. At zero CO conversion, the D_2-H_2 exchange rate (590 h^{-1}) is almost 20 times larger than the conversion rate (30 h^{-1}). It is also observed that the isotopic exchange nearly reaches equilibrium at CO conversions of 6-15%. Therefore, the results of the D_2-H_2 exchange experiment strongly suggest that the H_2 dissociation step is quasi-equilibrated during FTS.
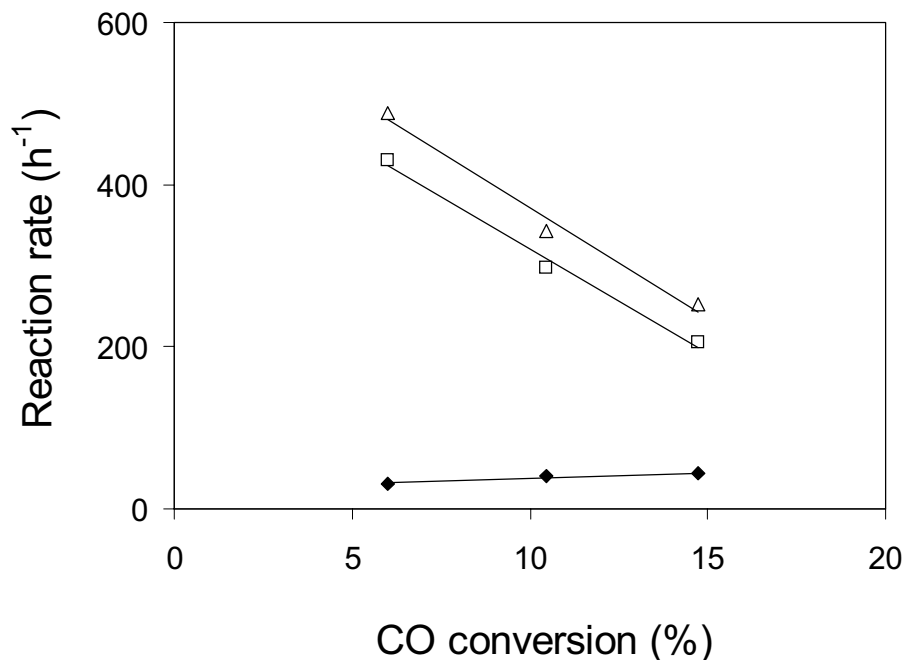

Figure 2.1. Rates of hydrogen converted to hydrocarbons (♦), HD formation (□) and equilibrium HD formation (Δ) in the D_2-H_2 exchange under FTS conditions on 21.9 wt.% Co/SiO_2 catalyst (200°C, 20 atm $H_2/D_2/CO = 1/1/1$).

D_2O tracer experiments were performed in the last quarter. Here we re-analyze some of the data from that experiment in Figures 2.2 and 2.3 and proposed some mechanistic implications for the observed water effects. During cobalt-catalyzed FTS, the removal of

oxygen adatoms (released from CO dissociation) occurs mainly via the formation of water in the following the steps [27].

O* + H* → OH* + *   (1)
OH* + H* → OH$_2$* + *   (2)
OH$_2$* ↔ H$_2$O + *   (3)
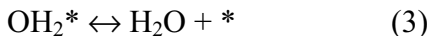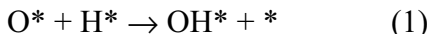
As a matter of fact, we found only trace amount of CO$_2$ and alcohols in the FTS products. In the mean time, water, either produced in FTS or added, may also adsorb on cobalt through the steps (3), (2) and (1) to produce OH$_2$*, OH*, H*, and O*. Figures 2.2 and 2.3 show that the deuterium content in the H$_2$ isotopomers, paraffins and olefins increases with increasing CO conversion by increasing bed residence time, indicating that the deuterium fraction in the surface H-D pool also increases with residence time. We assume that the water adsorption, step (3), is reversible and quasi-equilibrated. If this is the case, the following water dissociation, steps (2) and (1), should not be quasi-equilibrated. Otherwise, the deuterium content observed in the H$_2$ isotopomers and hydrocarbons would be independent of the residence time. When extrapolating the lines in Figures 2.2 and 2.3 to zero residence time, we obtain intercepts of about 0.03. This provides additional evidence that the steps (2) and (1) are not quasi-equilibrated, since the deuterium fraction in the reactants is 14%.
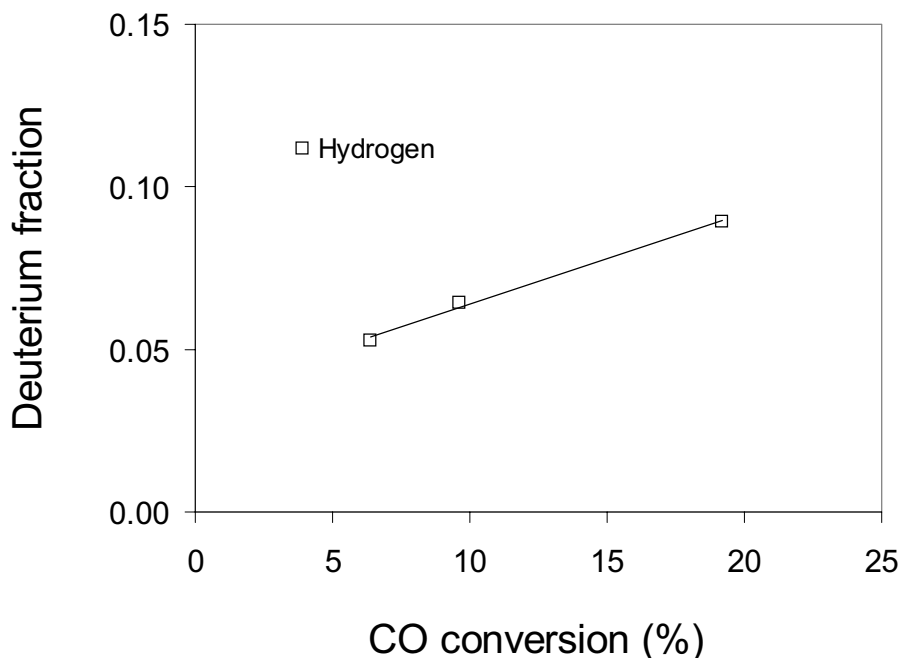

Figure 2.2. Deuterium fraction in hydrogen-isotopomers in FTS on 21.9 wt.% Co/SiO$_2$ catalyst (200°C, 20 atm H$_2$/CO = 2.0, 2 atm D$_2$O added).
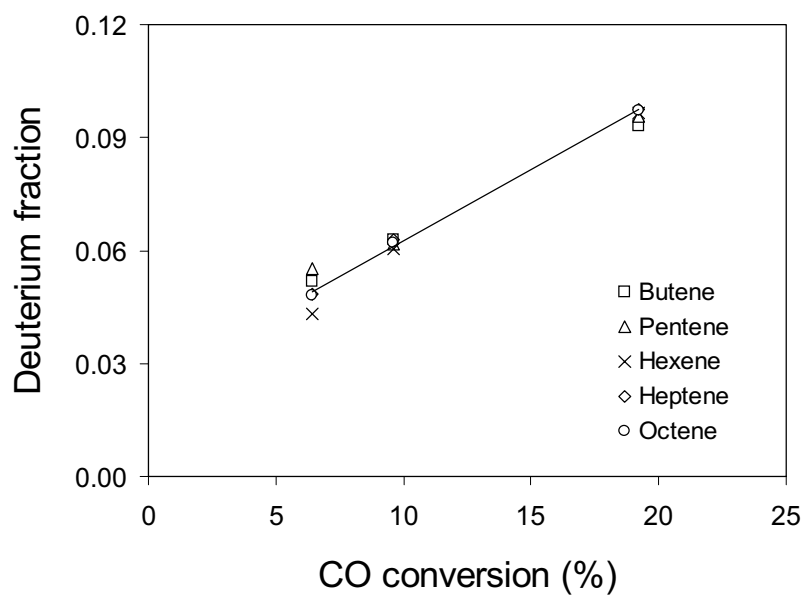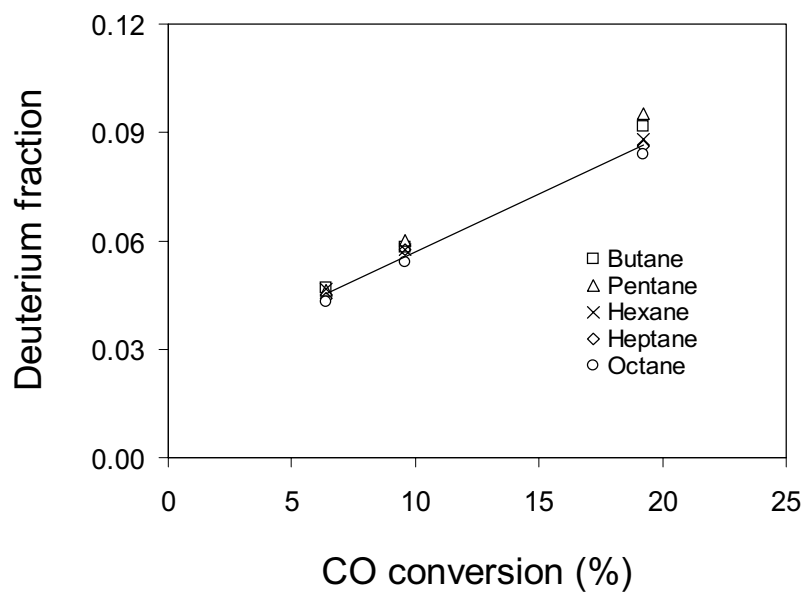
Figure 2.3. Deuterium fraction in paraffins olefins in FTS on 21.9 wt.% Co/SiO$_2$ catalyst (200°C, 20 atm H$_2$/CO = 2.0, 2 atm D$_2$O added).

3.2   Proposed Mechanism

The Fischer-Tropsch synthesis is a polymerization reaction, although the mechanism and the nature of the intermediates remain a subject of active discussion [13,27,28]. The surface carbide mechanism, which was originally proposed by Fischer and Tropsch [2], is the currently accepted route for the formation of monomers. This mechanism states that CO dissociates on the metal of catalyst to form carbon adatoms. Subsequently, carbon adatoms undergo hydrogenation to form surface methylene groups, which are the precursor to hydrocarbons with a broad range of chain length and functionality.

Table 2.1 Kinetic rate expressions of the FTS on cobalt-based catalysts

Reference	Catalyst	Overall kinetic expression*
van der Baan, *et al.,* [29]	Co/Al_2O_3	$-r_{CO} = aP_{H2}P_{CO}^{1/2}/(1 + bP_{CO}^{1/2})^3$
Wojciechowski, *et al.,* [25]	Co/Kieselguhr	$-r_{CO} = aP_{H2}^{1/2}P_{CO}^{1/2}/(1 + bP_{H2}^{1/2} + cP_{CO}^{1/2})^2$
Satterfield, *et al.,* [30]	$Co/MgO/SiO_2$	$-r_{CO+H2} = aP_{H2}P_{CO}/(1 + bP_{CO})^2$
Pannell, *et al.,* [31]	$Co/La_2O_3/Al_2O_3$	$-r_{CO+H2} = aP_{H2}^{0.55}P_{CO}^{-0.33}$
Yang, *et al.,* [32]	$Co/CuO/Al_2O_3$	$-r_{CO+H2} = aP_{H2}P_{CO}^{-0.5}$

* a, b, and c in these equations are temperature-dependent constants.

Some kinetic rate expressions FTS reported in the literature for cobalt-based are summarized in Table 2.1. According to these studies, the synthesis rate exhibits a positive order in H_2 while the influence of CO varies from negative to mildly positive depending on the CO concentration. However, none of these rate expressions contain a water partial pressure term, implying that these authors did not notice an effect of water. In these studies, the Langmuir-Hinshelwood type expressions were obtained by assuming that the rate-determining step involves the formation of surface methylene groups (CH_2^*) from adsorbed C^* and H^*. We observed the enhancement of the synthesis rate by water on cobalt catalysts. To explain the positive water effect, an additional pathway for C^* consumption had to be considered and this pathway must be influenced by gas phase water. From the D_2O tracer study, we know that the concentration of surface OH_2^* depends on the relative amount of water in the gas mixture. It is expected that surface C^* may react with OH_2^* to form $CHOH^*$ species. The latter species may be hydrogenated or reacts with partially hydrogenated Cn^* species through intermolecular dehydration. In fact, the presence of species containing C-O-H bands on cobalt FTS catalysts has been confirmed by IR spectroscopy [33]. Of course, other pathways may also lead to species containing C-O-H bands. The concentration of OH_2^* will increase with water partial pressure, increasing the C^* consumption through the proposed water-aided pathway. However, the hydrogenation of C^* using hydrogen remains operative and it is the

dominant route when the water concentration is low. The proposed elementary steps for FTS on cobalt are presented as follows:

1. $H_2 + 2* \leftrightarrow 2H*$
2. $CO + 2* \leftrightarrow C* + O*$
3. $C* + H* \rightarrow CH* + *$
4. $C* + OH* \rightarrow COH* + *$
5. $O* + H* \rightarrow OH* + *$
6. $OH* + H* \rightarrow OH_2* + *$
7. $OH_2* \leftrightarrow H_2O + *$

The dissociative H_2 adsorption (Step 1) is a quasi-equilibrated step (based on the results of D_2-H_2 exchange). In addition, it is not likely to be a rate-determining step because the FTS rate has a positive order in CO partial pressure for low CO concentrations [25]. CO chemisorbs molecularly and then dissociates to produce adsorbed C and O, respectively. The extent to which these processes are reversible remains unresolved [28]. In this work, we assume that CO adsorption (Step 2) is also quasi-equilibrated. We suppose two parallel pathways that consume surface C*, namely, C* reacting with H* (Step 3) and with OH_2* (Step 4). According to the D_2O tracer study, the water dissociation steps (steps 5 and 6) are largely irreversible, whereas the water adsorption/desorption (step 7) is quasi-equilibrated. Thus, we have the synthesis rate, $r_{-CO} = k_3[C*][H*] + k_4[C*][OH_2*]$. We assume that the important surface species are empty sites, and adsorbed C*, O*, OH_2* and H*. Other species, though present, are not important in the stoichiometric balance of surface sites. Applying the pseudo-steady state approximation to step 1 through 7 leads to a Langmuir-Hinshelwood type expression.

$$r_{-CO} = aP_{CO}{}^{1/2}P_{H2}{}^{1/4}(bP_{H2}{}^{1/2} + cP_{H2O})^{1/2}/(1 + dP_{H2}{}^{1/2} + eP_{H2O} + fP_{CO}{}^{1/2})^2 \text{, in which,}$$

$a = (K_1{}^{1/2}K_2\, k_5)^{1/2}$
$b = K_1{}^{1/2}k_3$
$c = k_4K_{-7}$
$d = (K_1)^{1/2}$
$e = K_{-7}$
$f = (K_2(k_5/k_3 + k_3/k_5))^{1/2}$

Since CO adsorption is much stronger than H_2 and water adsorption on cobalt [13,25], the term in the denominator containing CO partial pressure becomes much larger than the others if the relative amount of CO in the gas phase is not too low. Then, the rate expression simplifies to

$$r_{-CO} = aP_{CO}{}^{-1/2}P_{H2}{}^{1/4}(bP_{H2}{}^{1/2} + cP_{H2O})^{1/2} \text{, where,}$$

$a = k_1{}^{1/4}k_5{}^{1/2}/(K_2{}^{1/2}(k_5/k_3 + k_3/k_5))$
$b = K_1{}^{1/2}k_3$
$c = k_4K_{-7}$

3.3 Kinetic Study

Reaction kinetics of FTS was studied over a broad range of H_2/CO ratios (1.3 to 8.5) and pressures (13 to 33 atm). The experimental results are presented in Table 2.2. For this set of data, it was difficult to do a regression using only the two adjustable parameters, P_{CO}, P_{H2}. Thus, it was decided that the rate expression should contain another adjustable parameter, P_{H2O}. These data were first fitted using a multilinear regression, leading to a power law rate expression: $r_{-CO} = 56.3H_2^{0.43}CO^{-0.53}H_2O^{0.38}$.

This data will be regressed nonlinearly and fitted to a Langmuir-Hinshelwood type rate expression, which will be more representative of the true FTS mechanism on cobalt catalysts.

Table 2.2. Experimental results of FTS kinetic study over 21.9 wt.% Co/SiO_2 catalyst*

No	Partial pressure (atm)			CO conversion (%)	CO conversion rate (h⁻¹)	CH₄ formation rate (h⁻¹)	C₅+ synthesis rate (h⁻¹)
	H_2	CO	H_2O	(%)	(h^{-1})	(h^{-1})	(h^{-1})
1	11.6	5.4	0.5	17.2	48.3	4.6	41.8
2	11.6	5.7	0.3	8.7	36.9	4.2	28.7
3	9.3	6.0	0.2	7.7	29.9	2.8	24.1
4	18.3	6.0	0.1	4.5	32.3	5.8	17.8
5	17.2	5.1	0.6	20.4	64.7	8.8	53.7
6	17.9	5.9	0.2	8.0	42.5	6.6	29.8
7	24.0	5.3	0.5	16.6	70.4	12.1	51.1
8	25.0	6.0	0.2	7.6	50.1	10.0	29.3
9	11.9	5.8	0.2	7.4	41.8	5.2	32.2
10	11.3	5.3	0.6	21.3	59.7	5.2	50.8
11	11.9	5.9	0.2	6.6	37.2	5.2	27.5
12	10.8	2.6	0.3	20.4	57.2	7.3	42.7
13	11.5	2.8	0.1	7.7	43.9	8.0	30.8
14	10.2	2.3	0.5	32.9	68.6	9.4	58.1
15	11.8	5.8	0.2	5.3	30.1	4.4	22.2
16	11.4	5.5	0.5	17.1	54.0	4.9	43.4
17	11.2	5.2	0.6	21.5	60.4	5.4	50.4
18	11.4	1.4	0.1	10.0	57.0	13.1	--
19	10.6	1.3	0.2	23.1	64.7	12.6	--
20	9.7	1.2	0.3	38.5	80.3	16.4	60.4
21	11.3	5.2	0.6	20.4	57.2	5.3	47.5
22	11.6	8.7	0.2	4.8	27.4	3.2	20.6
23	11.3	8.6	0.3	6.6	30.4	3.0	22.9
24	11.7	5.4	0.5	18.0	50.5	5.1	42.5

* Reaction conditions: 200°C, H_2/CO ratios from 1.3 to 8.5, pressures from 13 to 33 atm, water partial pressure is the average of water pressures at the reactor inlet and outlet.

III. REFERENCE

1. M. E. Dry, The Fisher-Tropsch Synthesis, in *Catalysis-Science and Technology*, Vol. 1, p. 160, J. R. Anderson and M. Boudart eds., Springer Verlag, New York, 1981.
2. F. Fischer and H. Tropsch, *Brennstoff-Chem.* **7** (1926) 97.
3. R. B. Anderson, in *Catalysis* Vol. 4, p. 29, P. H. Emmett eds., Van Nostrand-Reinhold, New York, 1956.
4. H. H. Storch, N. Golumbic and R. B. Anderson, *The Fischer-Tropsch and Related Syntheses*, Wiley, New York, 1951; R. B. Anderson, *The Fischer-Tropsch Synthesis*, Wiley, New York, 1984.
5. H. Kolbel and M. Ralek, *Catal. Rev.-Sci. Eng.* **21** (1980) 225.
6. J. W. Niemantsverdriet and A. M. van der Kraan, *J. Catal.* **72** (1981) 385.
7. J. A. Amelse, J. B. Butt and L. J. Schwartz, *J. Phys. Chem.* **82** (1978) 558.
8. G. B. Raupp and W. N. Delgass, *J. Catal.* **58** (1979) 348.
9. R. Dictor and A. T. Bell, *J. Catal.* **97** (1986) 121.
10. J. P. Reymond, P. Meriaudeau and S. J. Teichner, *J. Catal.* **75** (1982) 39.
11. C. S. Kuivila, P. C. Stair and J. B. Butt, *J. Catal.* **118** (1989) 299.
12. C. S. Huang, L. Xu and B. H. Davis, *Fuel Sci. Tech. Int.* **11** (1993) 639.
13. E. Iglesia, and S. C. Reyes, R. J. Madon and S. L. Soled, *Advances in Catalysis*, Vol. 39, p. 221, Academic Press, 1993.
14. E. Iglesia, *Appl. Catal. A: General* **161** (1997) 59.
15. S. Soled, E. Iglesia and R. A. Fiato, *Catal. Lett.* **7** (1990) 271.
16. S. Soled, E. Iglesia, S. Miseo, B. A. DeRites and R. A. Fiato, *Topics in Catal.* **2** (1995) 193.
17. E. Iglesia, A research proposal submitted to the Division of Fossil Energy.
18. M. T. Xu, E. Iglesia, *J. Phys. Chem. B* **102(6)**, 961-966, 1998.
19. A. P. Raje, R. J. O'Brien and B. H. Davis, *J. Catal.* **180** (1998) 36.
20. A. F. Wells, *Structural Inorganic Chemistry*, Oxford, 1945.
21. D. B. Bukur, D. Mukesh, S. A. Patel, *Ind. & Eng. Chem. Res.* 1990, **29**, 194.
22. H. Kolbel, P. Ackermann, E. Rueschenburg, R. Langheim, F. Engekhardt, *Chem. Ing.Tech.* 1951, 23, 153-157.
23. *European Pat. Appl.* 201 557 (1983), assigned to Shell.
24. C. J. Kim, *European Pat. Appls*. 339 923 (1988) and 355 218 (1990), assigned to Exxon.
25. B. Wojciechowsky, *Catal. Rev. Sci. Eng.* **30** (1988) 678.
26. H. Schulz, M. Claeys, and S. Harms, *Stud. Surf. Sci. Catal.* **107** (1997) 193.
27. A. A. Adesina, *Appl. Catal. A: General* **138** (1996) 345.
28. A. T. Bell, *Catal. Rev. Sci. Eng.* **23 (1&2)** (1981) 203.
29. A. Outi, I. Rautavuoma, and S. van der Baan, *Appl. Catal.* **1** (1981) 247.
30. I. C. Yates, and C. N. Satterfield, *Energ. Fuel.* **5** (1991) 168.
31. R. B. Pannell, C. L. Kibby, T. P. Kobylinski, *Proc. 7th Int. Congr. Catal.* (1980) 447-459.
32. C. H. Yang, F. E. Massoth, and A. G. Oblad, *Adv. Chem. Ser.*, **178** (1978) 35-36.
33. H. H. Nijs, and P. A. Jacobs, *J. Catal.* **66** (1980) 401.

Task 12. Reporting/Project Management

Three monthly and one quarterly reports have been completed.